

THESIS FOR THE DEGREE OF DOCTOR OF PHILOSOPHY

INTEGRATED CIRCUIT DESIGN FOR HIGH  
DATA RATE POLYMER MICROWAVE FIBER  
COMMUNICATION

FRIDA STRÖMBECK



DEPARTMENT OF MICROTECHNOLOGY AND NANOSCIENCE  
CHALMERS UNIVERSITY OF TECHNOLOGY  
GÖTEBORG, SWEDEN 2023

Integrated Circuit Design for High Data Rate Polymer Microwave Fiber  
Communication  
FRIDA STRÖMBECK  
978-91-7905-807-4

© FRIDA STRÖMBECK, 2023.

Doktorsavhandlingar vid Chalmers tekniska högskola  
ISSN 0346-718X

Department of Microtechnology and Nanoscience  
Chalmers University of Technology  
SE-412 96 Göteborg, Sweden  
Telephone + 46 (0) 31 - 772 1000

Typeset by the author using L<sup>A</sup>T<sub>E</sub>X.

Printed by Chalmers Reproservice  
Göteborg, Sweden 2023

*Just because you don't know of a cure doesn't mean there isn't one. It's simply  
beyond your scope – Yennefer*



# Abstract

The rapid development of semiconductor processes with a maximum frequency of oscillation well above 300 GHz enables new applications at frequencies above 100 GHz to be researched and developed. Such applications include wireless backhaul, wireless access, radar and radiometer sensors, wireless energy distribution and harvesting, etc.

For several of these applications, a throughput in data rate well above 10 Gbps, even up to 100 Gbps, is required. Optical fiber communication is the leading option for high data rate and long-range wired communication. However, for shorter ranges like chip-to-chip or module-to-module (up to ten meters), millimeter-wave communication over a polymer microwave fiber (PMF) is an interesting alternative due to its potential low cost. Other advantages include flexibility, less sensitivity to temperature variations, and a more relaxed mechanical tolerance requirement. Similar to optical fiber, dispersion occurs on PMFs and will cause symbol interference. Different ways to deal with this effect are investigated, for example, pulse shaping and equalization of the signal.

This work proposes and presents various circuit solutions enabling high data rate communication. Two technologies are used, 250 nm InP DHBT and 130 nm SiGe BiCMOS. An energy-efficient solution using an RF-DAC and power detector for pulse amplitude modulated links are evaluated, as well as an I/Q modulated solution. I/Q (de-)modulators require more complexity, but the increased spectral efficiency can also increase the data rate further.

In summary, I explore the opportunities and challenges of short-range, ultra-high data rate, PMF bound communication, which is found to support 56 Gbps error-free ( $\text{BER} < 10^{-12}$ ) data and 102 Gbps with a  $\text{BER} = 2.1 * 10^{-3}$ .

**Keywords:** High Datarate, In-phase/Quadrature Modulation, Integrated Circuit Design, RF-DAC, Power Detector, Polymer Microwave Fiber, Pulse Amplitude Modulation,



# List of Publications

This thesis is based on the following appended papers:

**Paper A.** Frida Strömbeck, Zhongxia Simon He, and Herbert Zirath, *A RF-DAC based 40 Gbps PAM Modulator with 1.2 pJ/bit Energy Efficiency at Millimeterwave Band*, 2018 IEEE/MTT-S International Microwave Symposium - IMS, Philadelphia, PA, USA, 2018, pp. 931-933, doi: 10.1109/MWSYM.2018.8439488.

**Paper B.** Frida Strömbeck, Zhongxia Simon He, and Herbert Zirath, *Multi-Gigabit RF-DAC Based Duobinary/PAM-3 Modulator in 130 nm SiGe HBT*, The 15th European Microwave Integrated Circuits Conference (EuMIC), 2020.

**Paper C.** Frida Strömbeck, Mingquan Bao, Zhongxia Simon He, and Herbert Zirath, *Transmitter and Receiver Circuits for a High-speed Polymer-fiber based PAM-4 Communication Link*, Sensors, Special Issue; mm Wave Integrated Circuits Based Sensing Systems and Applications, 2022, doi: 10.3390/s22176645.

**Paper D.** Frida Strömbeck, Zhongxia Simon He, and Herbert Zirath, *Transmitter and Receiver for High Speed Polymer Microwave Fiber Communication at D-band*, IEEE Transactions on Circuits and Systems I: Regular Papers, Vol. 69, no. 11, pp. 4674 - 4681, Nov. 2022, doi: 10.1109/TCSI.2022.3197879.

**Paper E.** Frida Strömbeck and Herbert Zirath, *A PAM-4 Link for High Data Rate PMF Communication*, Asia-Pacific Microwave Conference (APMC 2022), Yokohama, Japan, 2022, pp. 55-57, doi: 10.23919/APMC55665.2022.9999803.

**Paper F.** Frida Strömbeck, Yu Yan, Zhongxia Simon He, and Herbert Zirath, *A 40 Gbps QAM-16 communication link using a 130 nm SiGe BiCMOS process*, 2022 IEEE/MTT-S International Microwave Symposium - IMS, Denver, CO, USA 2022, pp. 1013-1016, doi: 10.1109/IMS37962.2022.9865471.

**Paper G.** Frida Strömbeck, Yu Yan, and Herbert Zirath, *A Beyond 100 Gbps Polymer Microwave Fiber Communication Link at D-band*, submitted to IEEE Transactions on Circuits and Systems I: Regular Papers.

**Paper H.** Frida Strömbeck, Yu Yan, and Herbert Zirath, *An 80 Gbps QAM-16 PMF Link Using a 130 nm SiGe BiCMOS Process*, accepted to 2023 IEEE/MTT-S International Microwave Symposium - IMS, San Diego, CA, USA 2023.

---

Other Publications: The content of the following publications partially overlaps with the appended papers or is out of the scope of this thesis

**Frida Strömbeck**, Zhongxia Simon He, and Herbert Zirath, *AMCW Radar of Micrometer Accuracy Distance Measurement and Monitoring*, 2019 IEEE MTT-S International Microwave Symposium (IMS), Boston, 2019, pp. 1473-1475, doi: 10.1109/MWSYM.2019.8701002.

**Frida Strömbeck**, Zhongxia Simon He, Herbert Zirath and Dan Kuylenstierna, *Static Frequency Divider in GaN HEMT Technology*, 2021 European Microwave Conference - EuMC, London, UK, 2022, pp. 309-312, doi: 10.23919/EuMC50147.2022.9784244.

As part of the author's doctoral studies some of the work presented in this thesis has previously been published in [H]. Figures, tables and text from [H] may therefore be fully or partly reproduced in this thesis.

**H Frida Strömbeck**, *Integrated Circuit Solutions for High Datarate Polymer Fiber Communication*, Chalmers University of Technology, Gothenburg, 2021, ISSN 1652-0769.



---

# List of Acronyms

AC	–	Alternating Current
ADC	–	Analog-to-Digital Converter
AM	–	Amplitude Modulated
AWG	–	Arbitrary Waveform Generator
Balun	–	Balanced to unbalanced
BER	–	Bit Error Rate
BiCMOS	–	Bipolar Complementary Metal-Oxide-Semiconductor
DAC	–	Digital-to-Analog Converter
DC	–	Direct Current
DE	–	De-Emphasis
DHBT	–	Double Hetrojunction Bipolar Transistor
EM	–	Electromagnetic
FFT	–	Fast Fourier Transform
FIR	–	Finite Impulse Response
FSPL	–	Free Space Path Loss
Gbps	–	Gigabit per Second
GSG	–	Ground Signal Ground
HBT	–	Hetrojunction Bipolar Transistor
IC	–	Integrated Circuit
InP	–	Indium Phosphide
I/Q	–	In-phase / Quadrature
LNA	–	Low Noise Amplifier
LO	–	Local Oscillator
LSB	–	Lower Sideband
MMIC	–	Monolithic Microwave Integrated Circuit
mmW	–	Millimeter-wave
PAM	–	Pulse Amplitude Modulation
PD	–	Power Detector
PMF	–	Polymer Microwave Fiber
QPSK	–	Quadrature Phase Shift Keying
RF	–	Radio Frequency
RRC	–	Root Raised cosine
Rx	–	Receiver
SER	–	Symbol Error Rate
SiGe	–	Silicon Germanium
SNR	–	Signal to Noise Ratio
Tx	–	Transmitter
USB	–	Upper Sideband
VCO	–	Voltage Controlled Oscillator
WR	–	Rectangular Waveguide

# Contents

<b>Abstract</b>	<b>v</b>
<b>List of Publications</b>	<b>vii</b>
<b>List of Acronyms</b>	<b>ix</b>
<b>1 Introduction</b>	<b>1</b>
<b>2 High-Speed Short Distance Communication Systems</b>	<b>5</b>
2.1 Wireless Communication Systems . . . . .	5
2.2 Polymer Microwave Fiber . . . . .	7
2.3 Pulse Amplitude Modulation . . . . .	10
2.4 In-phase and Quadrature Modulation . . . . .	12
2.5 System Simulation . . . . .	15
2.5.1 Pulse shaping . . . . .	17
<b>3 Millimeterwave MMIC Technologies</b>	<b>19</b>
3.1 250 nm InP DHBT Technology . . . . .	19
3.2 130 nm SiGe BiCMOS Technology . . . . .	20
3.3 Design Considerations . . . . .	22
<b>4 Circuit Solutions for PAM Modulated Communication Systems</b>	<b>25</b>
4.1 Emitter Coupled Pair RF-DAC . . . . .	26
4.1.1 Duobinary/PAM-3 Modulator . . . . .	28
4.2 Stacked RF-DAC . . . . .	29
4.3 Power Detectors . . . . .	31
4.4 Comparator . . . . .	35
<b>5 Integrated Transceivers for I/Q Modulated Communication Systems</b>	<b>39</b>
5.1 Frequency Multipliers . . . . .	40
5.2 Mixers . . . . .	40
5.3 Amplifiers . . . . .	43
5.4 Integrated Tx and Rx Challenges . . . . .	43

<b>6</b>	<b>Evaluation of the Communication Systems</b>	<b>51</b>
6.1	PAM Modulated Tx/Rx in 250 nm InP DHBT Technology . . . . .	51
6.2	PAM Modulated Tx/Rx in 130 nm SiGe BiCMOS Technology . . . . .	53
6.3	I/Q Modulated Tx/Rx in 130 nm SiGe BiCMOS Technology . . . . .	56
6.4	Comparison with similar work . . . . .	59
<b>7</b>	<b>Conclusion and Future Outlook</b>	<b>61</b>
7.1	Conclusion . . . . .	61
7.2	Future Outlook . . . . .	61
<b>8</b>	<b>Summary of Appended Papers</b>	<b>63</b>
	<b>Bibliography</b>	<b>69</b>
	<b>Acknowledgments</b>	<b>73</b>
<b>I</b>	<b>Appended papers</b>	<b>75</b>
<b>A</b>	<b>A RF-DAC based 40 Gbps PAM Modulator with 1.2 pJ/bit Energy Efficiency at Millimeterwave Band</b>	<b>77</b>
<b>B</b>	<b>Multi-Gigabit RF-DAC Based Duobinary/PAM-3 Modulator in 130 nm SiGe HBT</b>	<b>83</b>
<b>C</b>	<b>Transmitter and Receiver Circuits for a High-speed Polymer-fiber based PAM-4 Communication Link</b>	<b>89</b>
<b>D</b>	<b>Transmitter and Receiver for High Speed Polymer Microwave Fiber Communication at D-band</b>	<b>105</b>
<b>E</b>	<b>A PAM-4 Link for High Data Rate PMF Communication</b>	<b>115</b>
<b>F</b>	<b>A 40 Gbps QAM-16 communication link using a 130 nm SiGe BiCMOS process</b>	<b>121</b>
<b>G</b>	<b>A Beyond 100 Gbps Polymer Microwave Fiber Communication Link at D-band</b>	<b>127</b>
<b>H</b>	<b>An 80 Gbps QAM-16 PMF Link Using a 130 nm SiGe BiCMOS Process</b>	<b>143</b>

# Chapter 1

## Introduction

The number of internet users is steadily growing. In 2020 the number of internet users surpassed 4 billion [16]. More and more essential services for our society depend heavily on functional network connections and communication systems. To meet the increasing demand for network services, new channels of communication and more efficient use of already utilized channels are vital. Different approaches are used for different applications, which is why we can see a variety of systems making up the internet [5].

From the everyday applications using mobile phones, streaming systems, and autonomous vehicles, high data rate connectivity is urgently needed even at a small distance. Data transfer between different central processing units (CPUs) within a local server must be quick and reliable. Some applications require temperature stability to be used in different environments. Others are limited by power, such as battery-driven devices, so power consumption becomes a major consideration.

There are plenty of benefits to transmitting data at a high data rate. As long as more errors in the transmission and a higher energy consumption per bit do not occur, one can argue that there are no direct disadvantages of a higher data rate. Of course, if requirements, like a wider bandwidth, are necessary to achieve said performance, pros and cons have to be considered. Sending the same amount of information but with a higher data rate will decrease the transmission time, thus reducing the transceiver's on-time, saving energy, and possibly enabling a longer lifetime of the device.

The channel bandwidth limits the amount of data that can be sent per time unit, which is limited by the response time of the active components (i.e. transistors). The response time is a consequence of the maximum frequency of oscillation of the component, so the technology is extremely important in high data rate systems. Other limiting factors are the strength of the signal compared to the noise of the surroundings and within the devices themselves. There is a theoretical limit of the maximum bit rate that can be transferred in an additive white Gaussian noise channel. In practice, the performance is always lower. Shannon's theorem gives the limit.

$$C = B \log_2 \left( 1 + \frac{S}{N} \right) \quad (1.1)$$



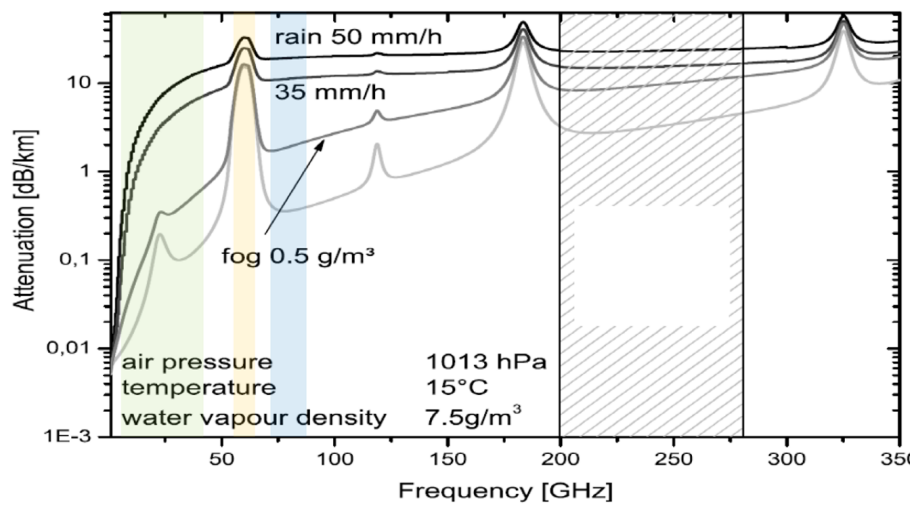


Figure 1.2: Atmospheric attenuation for different frequencies.

For wireless communication atmospheric attenuation has to be taken into consideration. Fig. 1.2 shows the atmospheric attenuation for different frequencies. For millimeter-wave frequencies, there is a window of low attenuation between 70-175 GHz and 200-300 GHz.

Looking at what data rate is required for different applications, for example, a fully autonomous car requires 24 Gbps [15]. Some of the challenges using millimeter-wave frequencies include limited output power, and therefore also, signal-to-noise ratio. Hardware such as analog-to-digital converters is limited as well.

## Thesis Outline

Following this introduction is chapter 2, which will discuss different options to achieve high-speed short-range communication systems. Following that is a chapter about the technologies used in this thesis. More details of circuit designs will be presented in chapter 4, which is about circuit solutions for pulse amplitude modulated communication systems. In chapter 5, the focus will be on circuit design for I/Q modulated communication links. Chapter 6 focuses on system performance. In chapter 7, a conclusion of this work and future goals can be found.



# Chapter 2

## High-Speed Short Distance Communication Systems

Both wireless communication using antennas and optical fiber communication is used today, because both systems have different advantages and drawbacks. A fiber optic system can reach far, but a wireless system is more flexible. This work focuses on short-range high data rate communication; thus, a brief introduction to wireless communication systems will follow.



### 2.1 Wireless Communication Systems

A wireless communication system is made of one part sending information using a transmitter (Tx) connected to an antenna and one part receiving the information through an antenna that feeds its signal to a receiver (Rx). The signal is, by definition, not wirebound between the antennas. The strength (power) of the signal that is received depends on the power of the signal that was sent, the directivity (i. e. how much the electromagnetic waves are focused in a specific direction) of the antennas, and the loss that occurs due to the spreading of the signal (free space path loss).

Friis' transmission equation can be used to calculate the amount of power transmitted from one antenna to the other [9].

$$P_r = \frac{G_t G_r P_t}{FSPL} \quad (2.1)$$

$P_r$  is the received power,  $P_t$  is the transmitted power,  $G_t$  is the antenna gain of the transmitting antenna,  $G_r$  is the antenna gain of the receiving antenna, and  $FSPL$  is

the free space path loss. The free space path loss can be calculated using

$$FSPL = \left( \frac{4\pi df}{c} \right)^2 \quad (2.2)$$

where  $d$  is the distance,  $f$  is the frequency and  $c$  is the speed of light. What limits the transmission is usually noise, primarily thermal noise from the receiver and the loss of the antenna.

The thermal noise power at the input of the receiver is given by;

$$N_0 = kTB \quad (2.3)$$

where  $k$  is Boltzmann's constant,  $T$  is the temperature of the antenna (which is the temperature of the object it is pointed at), and  $B$  is the signal bandwidth.

Signal-to-noise ratio (SNR) is a common measure within wireless communications. It is defined as;

$$\text{SNR} = \frac{P_{in}}{N_0} = \frac{E_b R_b}{n_0 B} \quad (2.4)$$

where  $N_0 = n_0 B$  is the noise power and  $E_b R_b$  is the digital signal power. Furthermore,  $\frac{R_b}{B}$  is the spectral efficiency.

The noise contributed by the component makes the SNR lower at the output of the said component. The change in SNR is defined as the component's noise figure (NF).

$$NF = \frac{\text{SNR}_{in}}{\text{SNR}_{out}} \quad (2.5)$$

For a cascaded circuit, the total noise figure is given by Friis' formula for noise;

$$NF = F_1 + \frac{F_2 - 1}{G_1} \quad (2.6)$$

where  $F_1$  is the noise figure of the first component,  $G_1$  is the gain from the first component, and  $F_2$  is the noise figure from the second component [4].

The symbol error rate depends on the SNR. A larger SNR gives a lower symbol error rate. A symbol can contain one or many bits, depending on the spectral efficiency of the modulation format.

Of course, the goal is error-free communication; thus, the noise should be kept low. For a larger bandwidth, the receiver picks up more thermal noise. At the same time, a large bandwidth means there can be a lower complexity of the modulation format (to obtain the same data rate). A lower modulation complexity means it is less sensitive to noise, which is why it requires a smaller SNR to remain error-free.

The other part of the SNR is the signal strength. Sending a strong signal is very beneficial, though not always easy. As the carrier frequency gets higher, power becomes a critical problem to obtain. The directivity of the antennas gets more important for the signal not to spread out, thus fade in strength. As the beam becomes smaller, the alignment between the antennas becomes increasingly tricky. The system will be more sensitive to vibrations and small effects that can cause miss-alignment. For short-range systems that require robustness, wirebound communication can be beneficial.

## 2.2 Polymer Microwave Fiber

Polymer microwave fibers (PMF) offer many benefits for short-range communication systems. The PMFs are flexible and made of low-cost plastics. Compared to optical fibers, the alignment to the PMF is much simpler because of the larger size of the PMF, which is why the PMF is a more robust solution. Furthermore, since the signal is mainly confined in and around the PMF, there are no legal frequency restrictions (due to the frequency allocation restrictions), which either limits the data rate or requires high modulation schemes, thus requiring high complexity. A higher complexity usually leads to high costs and high power consumption. The preferred propagating mode in the fiber is HE<sub>11</sub>, which is a hybrid mode with no cut-off frequency [36] [25].

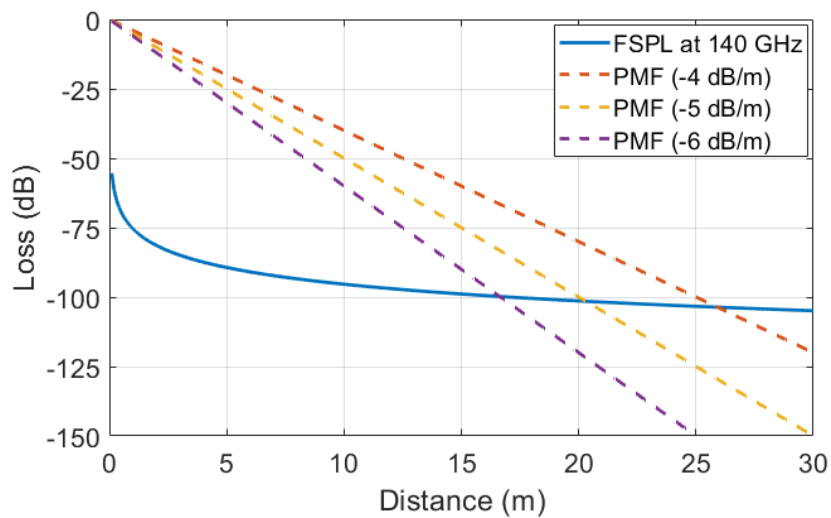


Figure 2.1: FSPL at 140 GHz compared to PMFs with 4,5 and 6 dB loss per meter.

Comparing short-range communication over PMF with air, the loss is less in the PMF for shorter distances which can be seen in Fig. 2.1. However, this figure does not include antennas but estimates the distances where a PMF may be beneficial.

An example of a PMF that was used during some measurements in this work was provided by Lehrstuhl für Hochfrequenztechnik (LHFT), University of Erlangen, Germany. A photo of the D-band (110-170 GHz) dielectric waveguide can be seen in Fig. 2.2. The length of the fiber is 1 meter, and it has a solid rectangular cross-section (1 mm by 2 mm) and is made out of high-density (with a density above  $0.930 \text{ g/cm}^3$ ) polyethylene (HD-PE). Examples of other polymers that can be used are polystyrene (PS), polytetrafluoroethylene (PTFE), and polypropylene (PP) [26].

Measurement of the S parameters ( $S_{11}$  and  $S_{21}$ ) of the fiber in Fig. 2.2 can be seen in Fig. 2.3. The measurement includes the loss of the transition to the waveguide on both sides.

One of the challenges with communication over PMF is the group delay, or more importantly, the difference in group delay for different frequencies. The varying

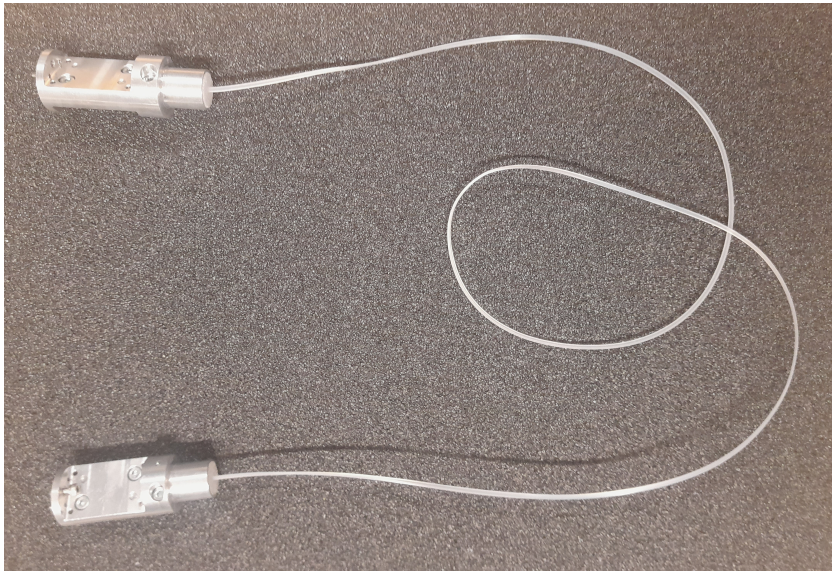


Figure 2.2: A 1-meter PMF with a solid rectangular cross-section (1 mm by 2 mm).

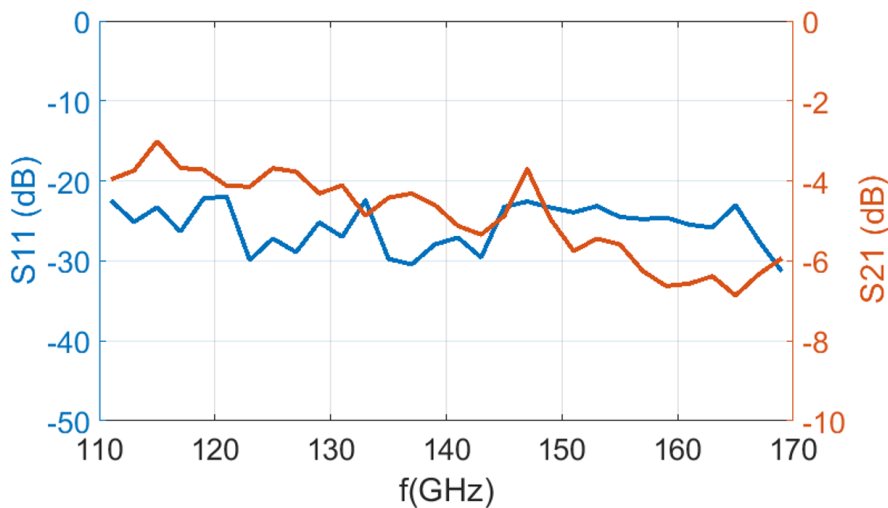


Figure 2.3: Measured S21 and S11 for the fiber, including the waveguide transitions.

group delay, called dispersion, degrades the signal and causes interference. In Fig. 2.4, the group delay of the measured fiber in Fig. 2.2 is shown.

The difference in group delay between 110 GHz and 170 GHz is about 0.6 ns (in Fig. 2.4). This has to be handled in some way for higher data rates with a wide bandwidth. De-emphasis and equalization are some ways to deal with this, which will be mentioned more in Section 2.5.

A fiber like the one in Fig. 2.2 has one major drawback. It is easily disturbed by the environment since the evanescent fields protrude the fiber core. A way to deal with this is by using foam-cladding around the core. An example of this type of fiber, also used during some measurements in this thesis, can be seen in Fig. 2.5. The

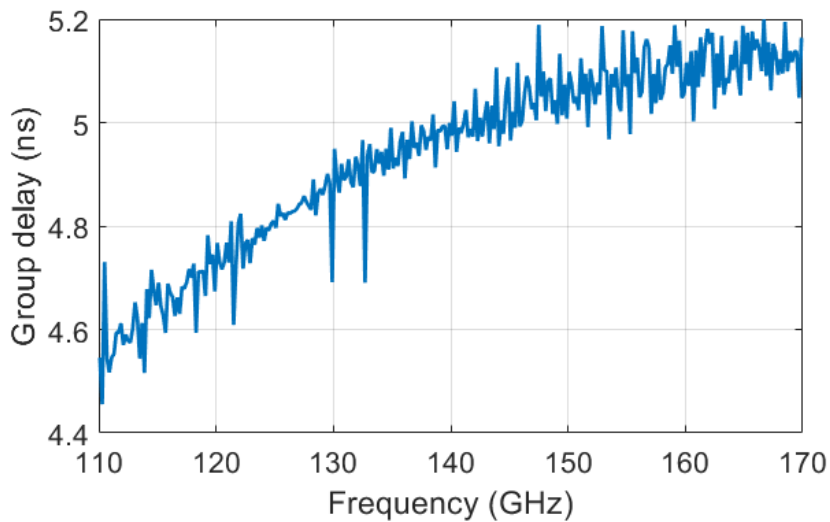


Figure 2.4: Measured group delay in the D-band.

fiber was provided by Huber+Suhner and had a rectangular polytetrafluoroethylene (PTFE) core that is 2.1 mm by 1.2 mm and a circular polyethylene (PE) foam cladding.



Figure 2.5: A 1 meter foam-cladded PMF with a solid rectangular cross-section (1.2 mm by 2.1 mm).

An adaptor was used to transfer the signal from and to the PMF to a rectangular waveguide. The inner core of the PMF was cut like a taper and inserted in the adaptor. A photo of the adaptor can be seen in Fig. 2.6.

Measured S-parameters including, adaptors can be seen in Fig. 2.7, and measured group delay is shown in Fig. 2.8.



Figure 2.6: The adaptor is used to transfer the signal from and to a rectangular waveguide.

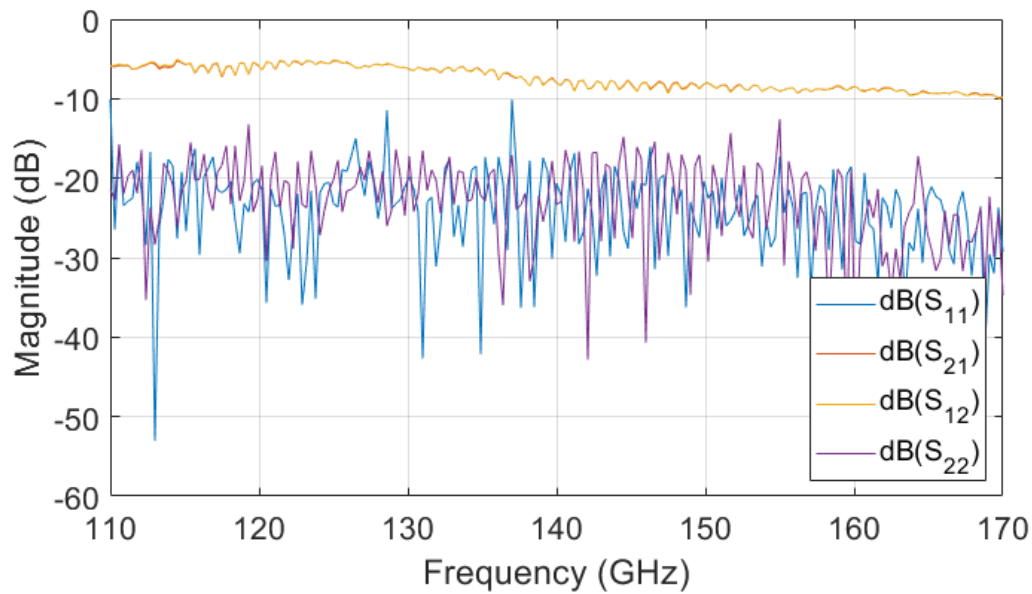


Figure 2.7: Measured S-parameters of the one-meter long PMF, including the transitions from waveguide to fiber and fiber to waveguide.

## 2.3 Pulse Amplitude Modulation

Pulse Amplitude Modulation (PAM) is a modulation format and can be either unipolar or bipolar. For a unipolar signal, all levels are non-negative, while a bipolar signal has evenly distributed levels where half of them are negative, and half of them are positive. A bipolar signal requires carrier recovery, while a unipolar signal can be demodulated using a simple power detector.

The transmitted unipolar PAM signal over one symbol period ( $0 \leq t \leq T$ ) is

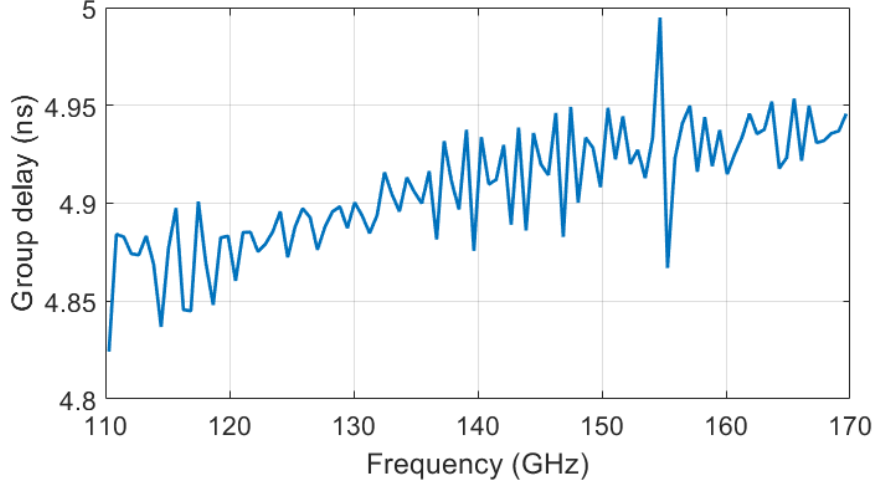


Figure 2.8: Measured group delay for the fiber, including waveguide transitions, for different frequencies at D-band.

given by

$$s_i(t) = A_i g(t) \sin(2\pi f_c t) \quad (2.7)$$

where  $A_i = (i - 1)d$ ,  $i = 1, 2, 3 \dots M$  for unipolar M-PAM,  $d$  is the amplitude separation distance between different levels,  $g(t)$  is a real-valued pulse shaping function, and  $f_c$  is the carrier frequency.

The symbol error probability for coherent unipolar M-PAM is given by;

$$P_s = \frac{2(M-1)}{M} Q\left(\sqrt{\frac{3(\log_2 M) E_b}{(2M^2 - 3M + 1) N_o}}\right) \quad (2.8)$$

where  $Q(\sqrt{2}x) = \frac{\text{erfc}(x)}{2}$ . Note that erfc is referring to the complementary error function [8].

The symbol error probability for incoherent unipolar M-PAM is given by;

$$P_s = \frac{1}{M} \left[ \exp\left(-\frac{1}{2}(\log_2 M) B_M \frac{E_b}{N_o}\right) + (2M - 3) Q\left(\sqrt{(\log_2 M) B_M \frac{E_b}{N_o}}\right) \right] \quad (2.9)$$

where  $B_M$  is given by;

$$B_M = \frac{3}{2M^2 - 3M + 1} \quad (2.10)$$

The difference between coherent and non-coherent demodulation becomes negligible when  $M$  becomes large.

While PAM-4 uses four different power levels, the ideal power levels are distributed in such way that a most significant bit (MSB) has double the power of the least significant bit (LSB), if your power detector has a linear response.

In Fig. 2.10, a PAM-4 modulated signal is shown and the corresponding demodulated waveform. An eye diagram of the demodulated signal with an indication of what bits are represented is also shown.

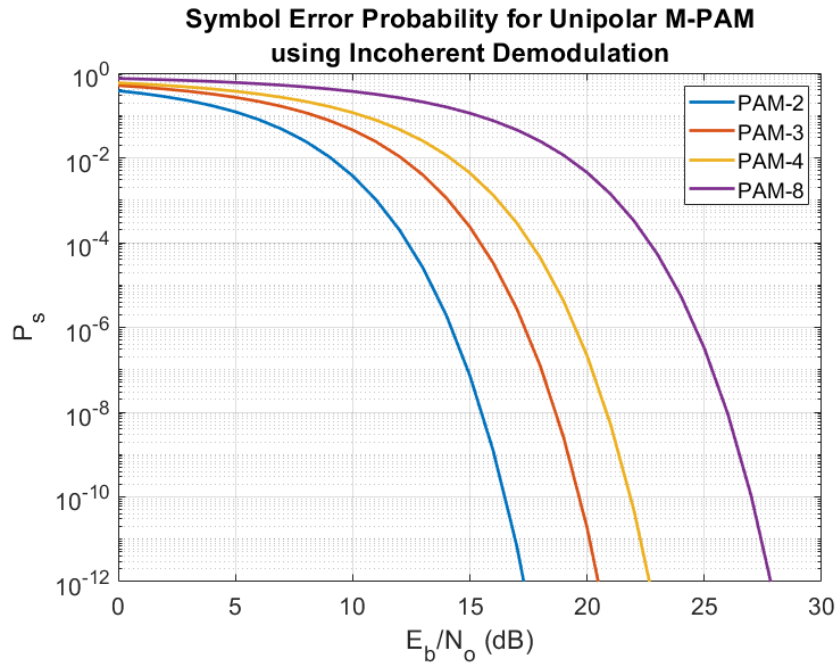


Figure 2.9

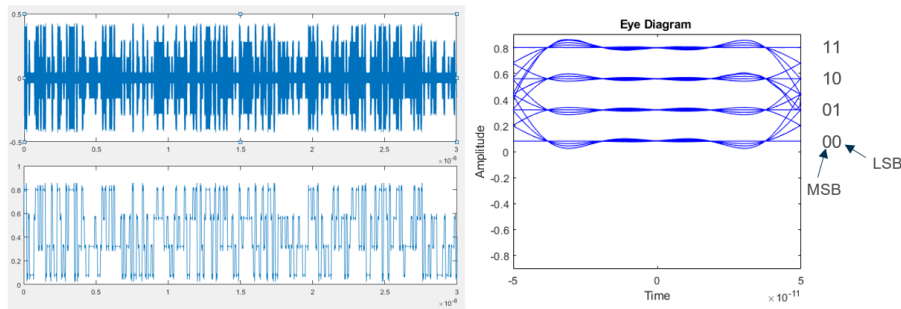


Figure 2.10: A PAM-4 modulated signal can be seen in the top left corner. The demodulated signal is shown in the bottom left corner. On the right side there is an eye diagram of the demodulated signal with corresponding bits.

## 2.4 In-phase and Quadrature Modulation

An in-phase and quadrature modulated signal consists of two signals combined with 90 degrees offset, one in-phase (I) component and one quadrature (Q) component. The signal can be plotted as a constellation with one component on each axis. The combination of the components will represent a symbol, that contains the information that represents the bits. In Fig. 2.11, a representation of the I/Q constellation diagram is shown.

An  $M$  - quadrature amplitude modulation (QAM) modulated signal has  $M$  different combinations of the I and Q signals. The amount of bits being sent per symbol is given by  $n$ , where

$$M = 2^n \quad (2.11)$$

thus a QPSK (4-QAM) signal is sending 2 bits per symbol.

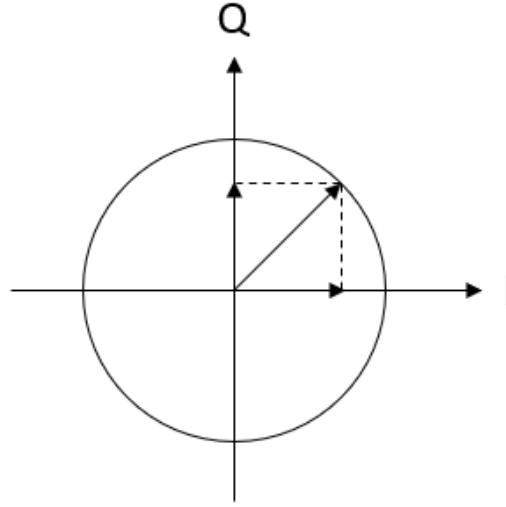


Figure 2.11: I/Q constellation.

The signal transmitted for one symbol period ( $0 \leq t \leq T$ ) is given by

$$S_i(t) = \sqrt{\frac{2E_0}{T}} a_i \cos(2\pi f_c t) + \sqrt{\frac{2E_0}{T}} b_i \sin(2\pi f_c t) \quad (2.12)$$

where  $E_0$  is the energy of the signal with minimum amplitude.  $a_i$  and  $b_i$  are independent integers ( $-\sqrt{M} + 1 \leq a_i \leq \sqrt{M} - 1$ ), ( $-\sqrt{M} + 1 \leq b_i \leq \sqrt{M} - 1$ ).

The bit error probability for an M-QAM signal is given by

$$P_b = \frac{4}{n} \left(1 - \frac{1}{\sqrt{M}}\right) Q\left(\sqrt{\frac{3n}{M-1} \frac{E_b}{N_0}}\right) \quad (2.13)$$

and the bit error probability for different  $E_b/N_0$  is plotted for QPSK, QAM-16 and QAM-64 in Fig. 2.12.

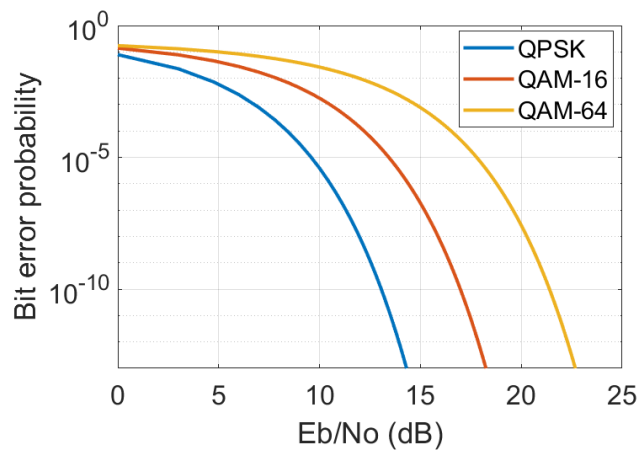


Figure 2.12: Bit error probability for different quadrature amplitude modulation orders.

It is important to note that the bit error probability is different than the symbol error probability, since only one bit in the symbol may be wrong, while the rest is correct.

Looking at the architectures of transmitters and receivers to transfer the QAM modulated signals, the simplest is using direct conversion, meaning the signal is mixed with the carrier directly. Benefits include that an image frequency is avoided, smaller, thus cheaper circuits, and lower energy consumption. Looking at the circuit design, direct conversion needs more careful design to avoid, for example LO leakage.

A simple block diagram of an I/Q transmitter is illustrated in Fig. 2.13, and Fig. 2.14 is the block diagram of the receiver. For the transmitter, the LO is split into two with a phase shift of 90 degrees, then mixed with the baseband signal (I/Q) to be upconverted. The down-conversion works the same way, but instead, the RF is mixed with the LO and a baseband signal can be extracted. The LO signals of transmitter and receiver should be synchronized, since both phase and amplitude is important for a I/Q modulated signal.

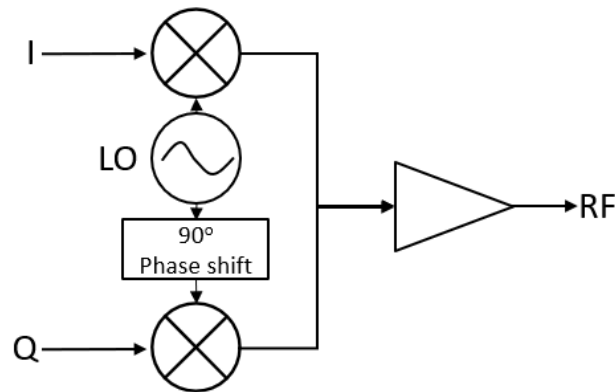


Figure 2.13: I/Q transmitter using direct conversion. The LO is the carrier frequency.

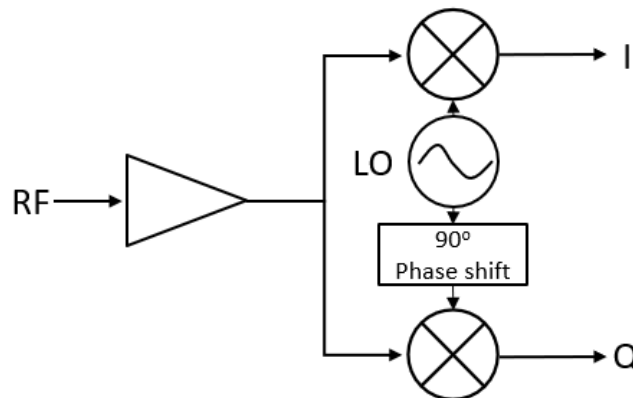


Figure 2.14: I/Q receiver using direct conversion. The LO is the carrier frequency.

## 2.5 System Simulation

The effects of the fiber on a PAM-4 signal was simulated to understand the limitations and important parameters of the system. Matlab was used for the system simulations, and CST Studio Suite was used to simulate the fiber. The electromagnetic (EM) simulation showed the propagation of the signal (Fig. 2.15). A scattering (S) parameter file was created, which was used to predict the effects of the PAM-4 signal.

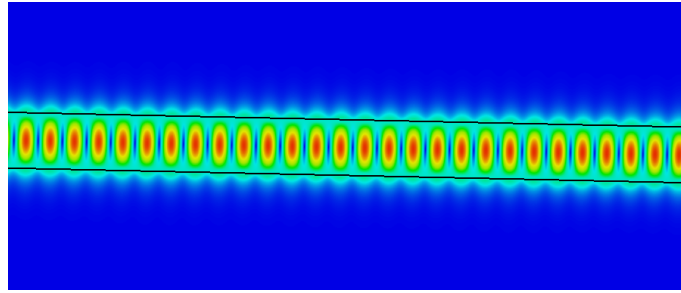


Figure 2.15: CST was used to simulate the propagation of the signal through the fiber at D-band. The frequency was set to 140 GHz in this figure.

Polytetrafluoroethylene (PTFE) was used as fiber material and the dimensions were 1x2mm in the simulation. Simulated S21 and group delay can be seen in Fig. 2.16 and Fig. 2.17. The simulations of the fiber did not include any transition to and from the fiber.

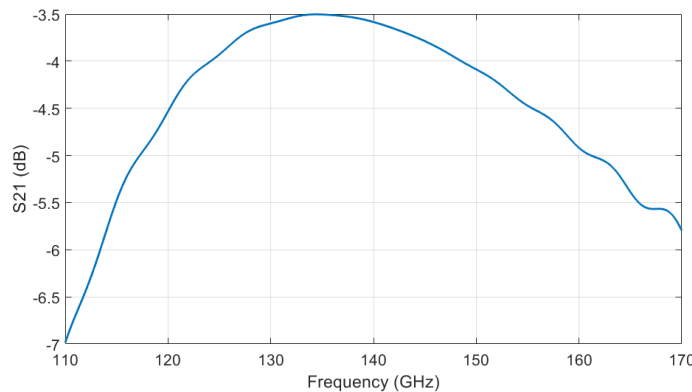


Figure 2.16: CST simulated S21 of a 1 meter long PTFE fiber.

Random data ( $D$ ) is generated and up-sampled. An oversampling of 400 per symbol was used during these simulations. The data was given an amplitude in voltage ( $A_V$ ), a constant amplitude of leakage ( $A_I$ ) was added, which is independent to the data. The amplitude is multiplied with the sinusoidal carrier, resulting in a modulated signal ( $y$ ).

$$y = (A_I + A_V D) \sin(2\pi f_c t) \quad (2.14)$$

The signal is converted to frequency domain using fast fourier transform (FFT), and the transfer function generated from the s-parameters of the PMF is applied to

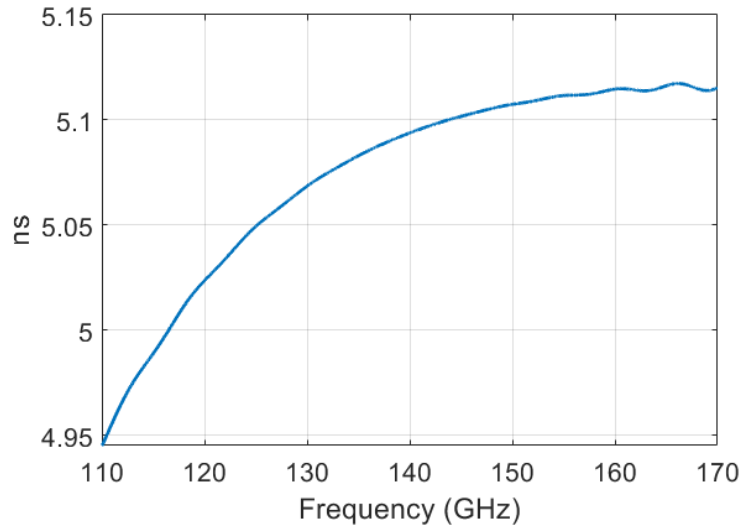
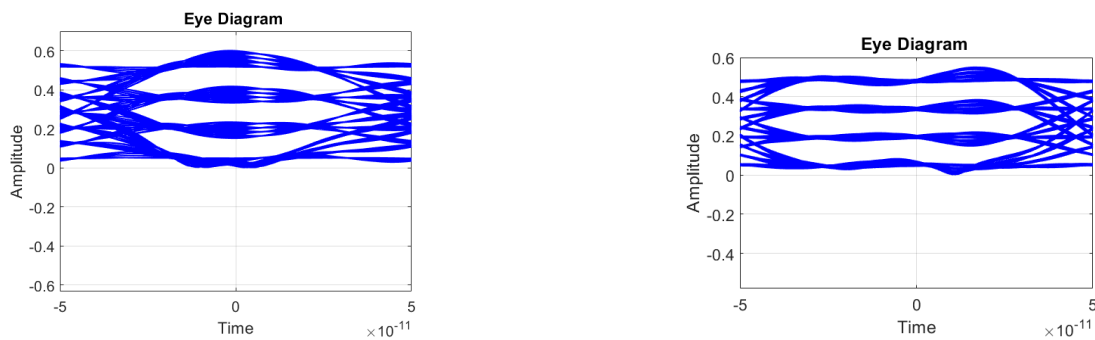


Figure 2.17: CST simulated group delay of a 1 meter long PTFE fiber.

the signal. The signal is then converted back to time domain, using inverse FFT. The envelope of the output signal is down-sampled, and the amplitude is compared to recover the output bitstream.

Simulations with a carrier frequency of 135 GHz, where the attenuation is the lowest and the difference in attenuation over the bandwidth of the signal is minimized, were compared to simulations with 150 GHz as the carrier, where the group delay difference is significantly lower over the bandwidth of the signal. The eye diagrams of the demodulated PAM-4 signal for the different carrier frequencies can be seen in Fig. 2.18. The Baud rate was 10 GBd for both carriers, and the fiber was 1 meter long. Rectangular pulse shaping was used.



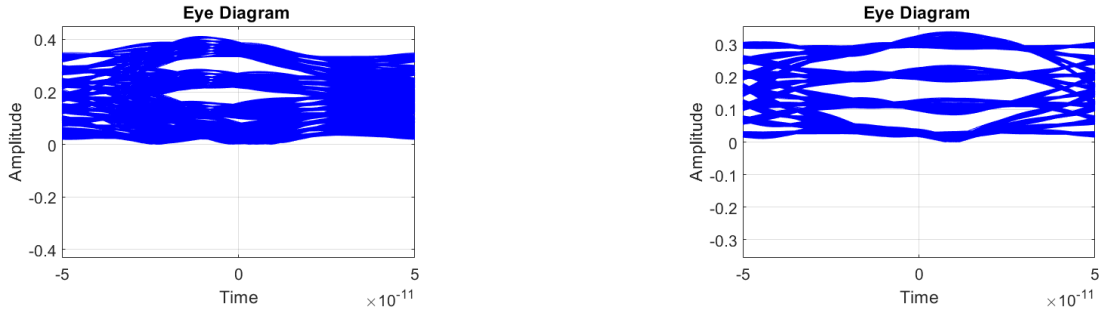
(a) Eye diagram of a demodulated 10 GBd PAM-4 signal using a carrier at 135 GHz over the simulated 1 meter long fiber.

(b) Eye diagram of a demodulated 10 GBd PAM-4 signal using a carrier at 150 GHz over the simulated 1 meter long fiber.

Figure 2.18: Eye diagrams of a demodulated transmissions over 1 meter pmf. The amplitude unit is volt, and the time unit is seconds.

The difference in the shape of the eye diagrams are noticeable. The lower carrier frequency has more widening of the eye diagram, due to the difference in group delay.

To get a clearer view of the effects, same simulations were made, but over a 2 meter long fiber. The eye diagrams can be seen in Fig. 2.19.



(a) Eye diagram of a demodulated 10 GBd PAM-4 signal using a carrier at 135 GHz over the simulated 2 meter long fiber.

(b) Eye diagram of a demodulated 10 GBd PAM-4 signal using a carrier at 150 GHz over the simulated 2 meter long fiber.

Figure 2.19: Eye diagrams of a demodulated transmissions over 2 meter PMF. The amplitude unit is volt, and the time unit is seconds.

The difference in group delay for different frequencies (dispersion) of the fiber is a critical limitation. From the simulations one can see that the dispersive effects are lower at high carrier frequencies for the PMFs. From that point of view, it is beneficial to use a high carrier frequency. Further more, moving up in frequency face other challenges, like power limitations.

### 2.5.1 Pulse shaping

The fiber changes the signal's shape, and the ideal output signal has the shape of the input signal. If the input signal is used as output and the inverse transfer function (of the fiber) is used to calculate the input, the ideal input signal can be retrieved. In Fig. 2.20 the shape of the simulated input signal can be seen. The carrier used in the simulation is 150 GHz and the bit rate is 15 Gbps PAM-2 signal.

The lower frequencies are attenuated, giving a sharper edge if the bit is switched. De-emphasis can be used on the transmitter side to achieve this effect, and the pulse shaping using one negative post cursor tap can be seen in Fig. 2.21.

Compensation for the distortion of the signal can also be done at the receiver side, using an equalization filter (equalizer). The easiest implementation of an equalizer is a high pass filter, that will attenuate the lower frequencies of the signal, and in that way equalize the signal.

An other approach is to try to minimize the signal's bandwidth by using pulse shaping, such as raised-cosine (RC) or root-raised-cosine (RRC). In Paper D and Paper E, different pulse shaping is used to evaluate the benefits.

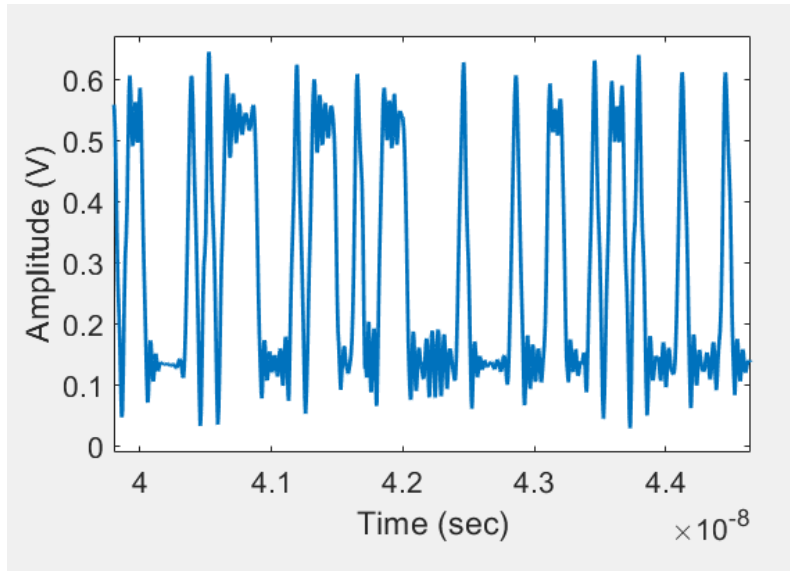


Figure 2.20: Using the inverse transfer function of the fiber to achieve the ideal input signal. The data rate is 15 Gbps and the carrier frequency during the simulation is 150 GHz.

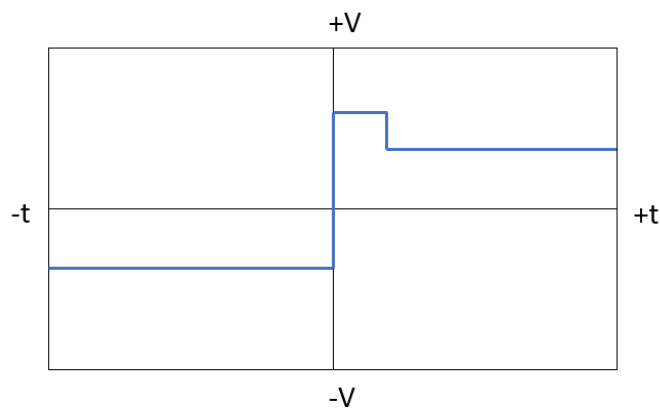


Figure 2.21: De-emphasis with one negative post cursor tap.

# Chapter 3

## Millimeterwave MMIC Technologies

In this work mainly two different technologies has been used, one developed by Teledyne scientific company and the other by Infineon technologies.

### 3.1 250 nm InP DHBT Technology

Teledyne Scientific Companies Indium Phosphide (InP) heterojunction bipolar transistor (HBT) process TSC250 is an advanced bipolar process that relies on sub-micron transistor scaling to achieve a state-of-the-art device performance. Devices in the technology offer typical RF figures-of-merit ( $f_t$  and  $f_{max}$ ) of 350/600 GHz while maintaining a common-emitter breakdown voltage ( $BV_{CEO}$ ) of greater than 4V. The wide bandwidth and high power handling capability of the devices make the technology ideally suited for next generation millimeter-wave, mixed-signal and digital integrated circuits.

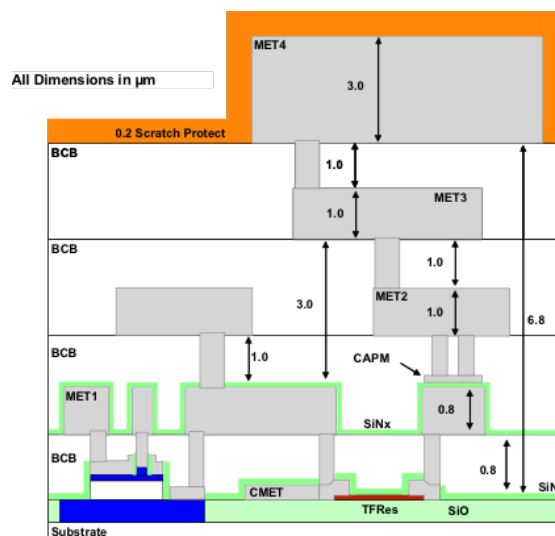


Figure 3.1: Representative cross-section of TSC250 IC technology. Drawing is not to scale. *Courtesy: Teledyne Scientific Company*

The technology has 4 metal layers, M1, M2, M3 and M4. The dielectric constant of the interlayer dielectric (BCB) is estimated to be  $\epsilon_r = 2.7$ . A cross-section drawing can be seen in figure 3.1.

Using a thin layer of Silicon Oxide (SiO), that sits on the InP substrate, thin-film resistors are formed. The metal-insulator-metal (MIM) capacitors are formed between M1 and the capacitor metal (CAPM) with a 200 nm Silicon Nitride (SiN) dielectric layer in between.

Each layer has a maximum current density that cannot be exceeded. Metal 1 has  $4\text{mA}/\mu\text{m}$ , metal 2 and 3 has  $5\text{mA}/\mu\text{m}$ , metal 4 has  $15\text{mA}/\mu\text{m}$  and the thin-film resistor has  $1\text{mA}/\mu\text{m}$ . The vias connecting different layers also has limits for the current.

The design kit includes two types of transistors; standard devices, and single-sided collector contact devices. The single-sided collector device has a collector contact on only one side of the base mesa. This results in approximately a 2x increase in the collector resistance, but reduces the footprint of the transistor by approximately 30%. The estimated safe operating area for the devices can be seen in 3.2.

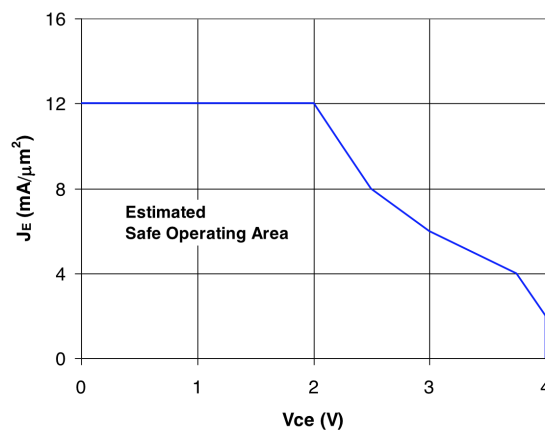


Figure 3.2: Estimated safe operating area for 250nm HBT devices in common-emitter configuration. The current density is given by  $J_E = \frac{I_C}{(0.25 \times \text{Emitter length})}$ .  
*Courtesy: Teledyne Scientific Company*

A design kit for TSC250 was available for Keysight ADS to simulate the predicted performance.

In Fig. 3.3 a few of the components in the TSC250 process is displayed.

## 3.2 130 nm SiGe BiCMOS Technology

The Silicon Germanium (SiGe) BiCMOS technology consists of two different transistor types, the heterojunction bipolar transistor (HBT) and metal oxide semiconductor field effect transistors (MOSFETs) that come in p- and n-channel varieties to create a complementary set (CMOS). CMOS enables low power logic operation, while the HBTs is for high speed analog components. Infineon's 130 nm SiGe BiCMOS process (B11HFC) that is used in this work include npn transistors with  $f_t/f_{\max}$

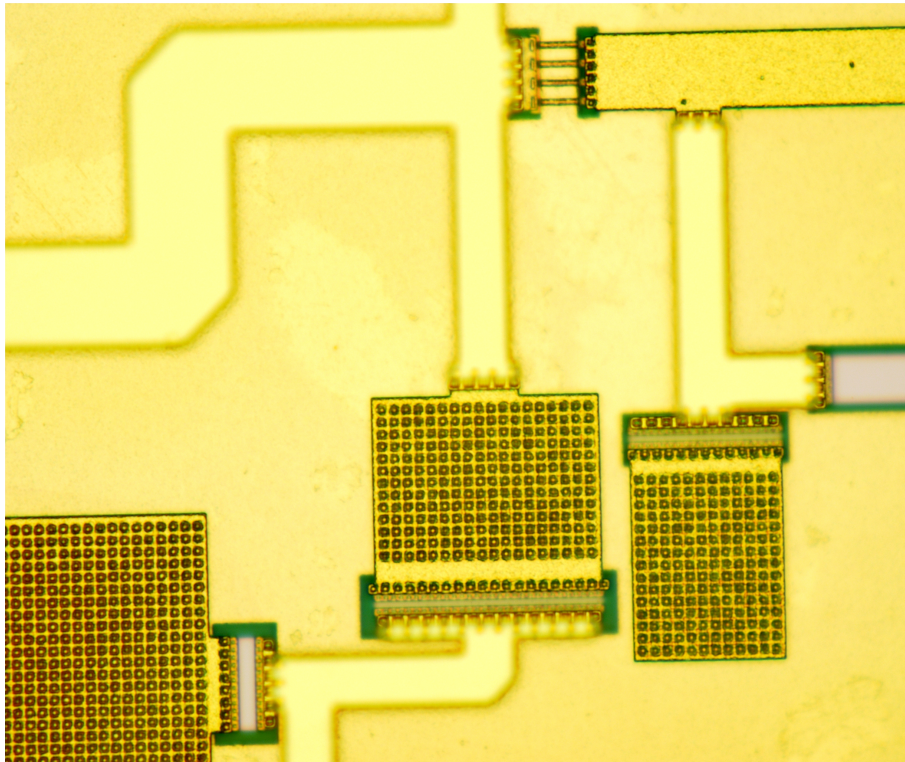


Figure 3.3: The TSC250 process. On the top a transistor can be seen connected to transmission lines. The large squares are capacitors.

of 250/400 GHz. A cross-section of the technology can be seen in Fig. 3.4. The technology also include thin film resistors, metal-insulator-metal (MIM) capacitors, junction capacitors, pin diodes and six layers of copper based interconnects (M1-M6). M1-M4 are thinner layers compared to M5-M6 which are used as the top layer of the microstrip lines for RF routing. M4 is used as the ground layer in most cases (some passive components like phase shifters may use another ground layer) [3].

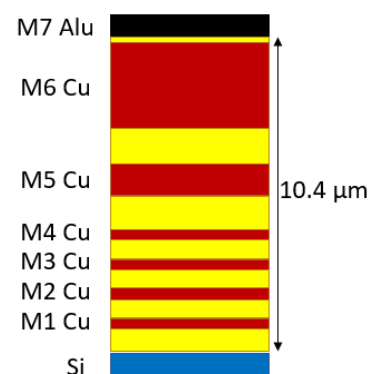


Figure 3.4: The metal stack of Infineon's B11HFC technology.

A design kit for B11HFC was available for Cadence to simulate the predicted performance.

### 3.3 Design Considerations

It is important to understand that  $f_t$  (transition frequency) and  $f_{max}$  depends on the current density. For most III-V and SiGe HBTs, these peaks ( $f_t$  and  $f_{max}$ ) occur for the same current density. For high datarate designs it is crucial to bias the transistors to the correct current.

In some processes there are density requirements, like in Infineon's SiGe processes. That means there has to be a certain metal concentration (in the case of B11HFC it's between 15 and 85% of each metal layer). Metal is added to fulfill the density requirements which means attention has to be paid to keeping the metal density correct in the designed circuit. A filling pattern can be seen in Fig. 3.5, where different squares of metal is applied around the RF-path of the circuit.

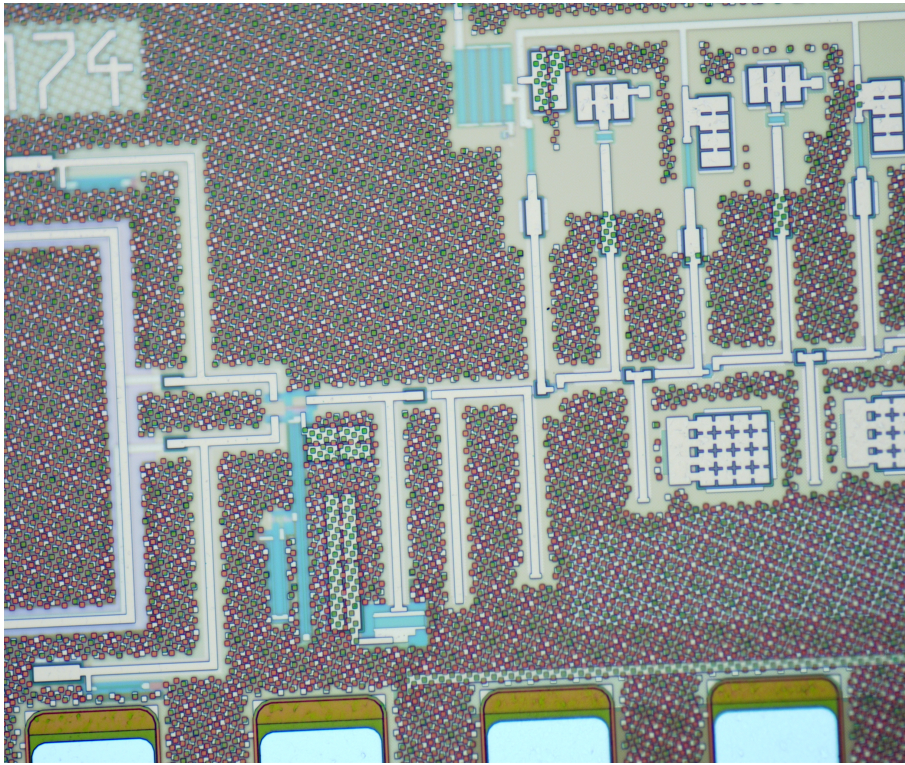


Figure 3.5: Metal filling in Infineon's B11HFC technology.

Magnification of the different metal layers can be seen in Fig. 3.6.

The ground is never an ideal ground, but is more accurately modeled as a small resistance or inductance to the ground, thus balanced circuits may be beneficial because the grounding is less important. When connecting signals between metal layers vias are used, which also include a small inductance. Passive elements like thin-film resistors include capacitance to ground, which is why the size of the component becomes important. Capacitors will also include capacitance to ground, as well as some series resistance and inductance. Corner cases like extremely small or very large components may differ in reality from the model provided by the foundry [22].

For high frequency design it gets challenging, because not many models are developed and guaranteed to agree at frequencies above 100 GHz. Small changes in

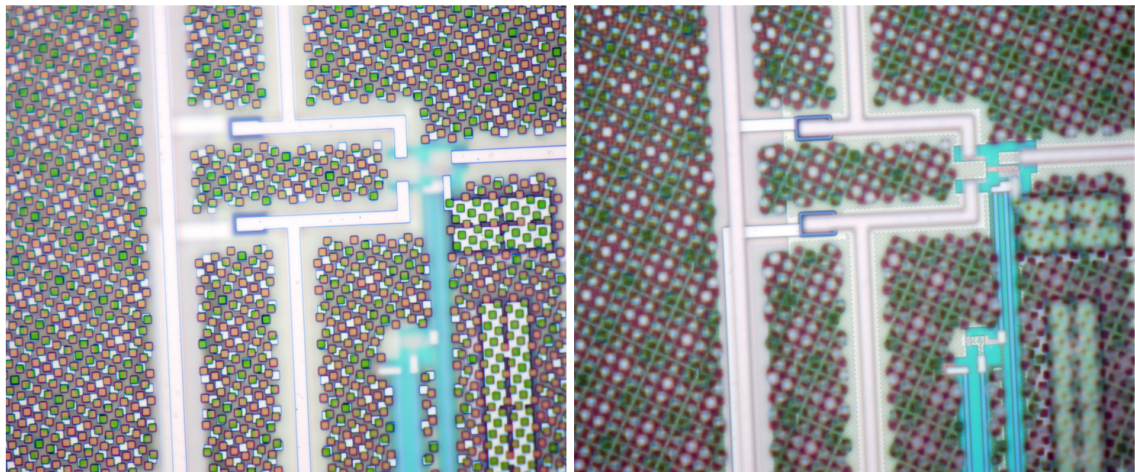


Figure 3.6: Zooming in on different layers of the B11HFC technology.

features of the high frequency circuits will have a much larger impact, because they are larger in comparison to the wavelength.



## Chapter 4

# Circuit Solutions for PAM Modulated Communication Systems

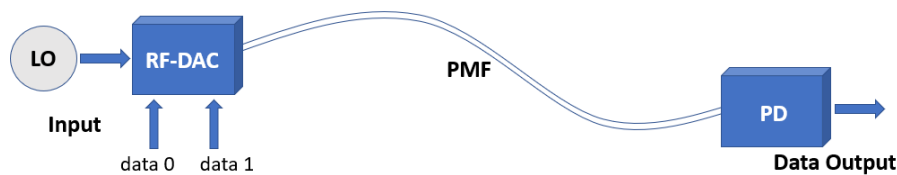


Figure 4.1: Overview of a PAM-4 modulated system using an RF-DAC and power detector.

Looking at some of the possible parts of a PAM communication system a local oscillator (LO) is required. It can either oscillate at the carrier frequency of the system or an X-times lower frequency and be followed by a frequency multiplier. At higher frequencies it is challenging to achieve oscillators with high output power. Off-chip oscillator can be used, but then there is a challenge to transfer the signal to the chip.

A radio-frequency digital-to-analog converter (RF-DAC) can be used as a PAM modulator. The RF-DAC uses an LO at desired carrier frequency and modulates the power depending on the data bits that are applied to the RF-DAC. For PAM-4 the RF-DAC uses two data input ports and modulates the signal to four different power levels. In Fig. 4.1 a simple PAM-4 modulated system including an RF-DAC and PD is displayed. A power amplifier (PA) can follow the output of the RF-DAC.

The transition from the chip to the PMF, and from the PMF to the chip is an important part of the system. Several different solutions are presented in [25] [35] [32] [31] [18] [13].

On the receiver side, the first stage can be a low noise amplifier (LNA). The demodulation is in part done a power detector (PD), which delivers an output voltage corresponding to the power that is fed at the input. For a PAM-4 signal four different

voltages, one for each possible symbol, is received. To be able to receive a single bit stream one can use comparators.

In this chapter, the focus will be on the RF-DAC and the PD.

## 4.1 Emitter Coupled Pair RF-DAC

For high-speed solutions current steering is the most commonly used technique to create an "On-Off"-switch. This can be done by using a differential pair [34].

The design topology adopts emitter coupled pair (ECP) as a gain control. By using two of such ECP structure, the local oscillator (LO) input can be converted into PAM modulated millimeterwave output. The ECP structure can regulate the output amplitude at a high switching rate (high data rate) as well as ensure good output linearity for PAM operation.

In Paper A an RF-DAC based PAM-4 modulator was designed and fabricated in the TSC250 InP technology. The frequency range for the circuit covered E-band (60-90 GHz) The simplified schematic of the proposed modulator is illustrated in Fig. 4.2. Two ECP structures are used for most significant bit (MSB), D0, and the least significant bit (LSB) D1 respectively. The ECP for MSB includes transistor E1-E4 (transistor size:  $3 \mu\text{m}$  for E1 and E4,  $8 \mu\text{m}$  for E2 and E3), and the transistors E5-E8 (transistor size:  $3 \mu\text{m}$  for all) are used for LSB. The LO input signal is given at the base of E1 and E5, while both E1 and E5 are configured as emitter followers,  $R_7=R_9=100 \text{ Ohm}$  are used to achieve wide band matching after power split.

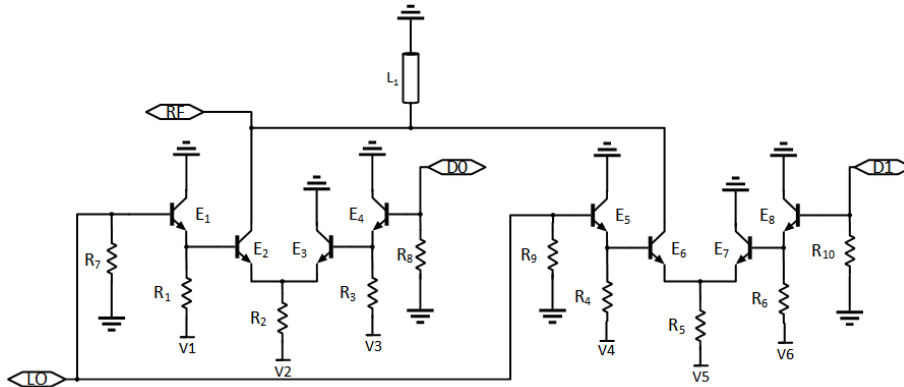


Figure 4.2: A simplified schematic of the ECP RF-DAC circuit.

The design of the RF-DAC is based on using differential pairs as a way to control the output power of the signal. When MSB bit '1' (0 V as logic '0' and 0.3 V as logic '1') is presented at the base of E4, it would steer the current away from E2 therefore reduce the output amplitude. Similar mechanism is applied to the other ECP, however with scaling of the transistor E6 and E7 act as LSB. The collectors of E2 and E6 are connected and shared a common inductor L1 (realized by a  $240 \mu\text{m}$  microstrip line) to generate RF output. The photo of the fabricated MMIC is shown in the Fig. 4.3.

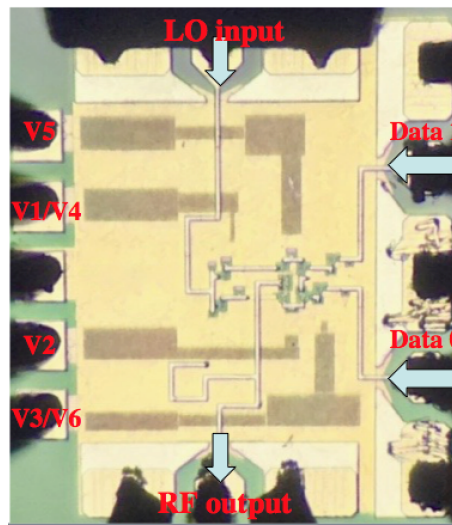


Figure 4.3: The photo of the RF-DAC. The chip size is  $800\mu\text{m} \times 800\mu\text{m}$ .

Time domain measurements using a Lecroy LabMaster 10-100Zi real-time oscilloscope to capture output RF signal, demonstrated capability to transmit a PAM-4 signal at data rates up to 40 Gbps. At 40 Gbps the bit error rate (BER) was measured to be  $3.7 \times 10^{-6}$ , and the dc energy efficiency was 1.2pJ/bit. The peak output power of the RF-DAC was measured to be -5 dBm at 75 GHz.

In Paper C a similar design was used, but shifted to F-band (90-140 GHz). Instead of using transistor scaling, to create a MSB and LSB, complete symmetry was used, but different emitter voltages for the pairs were used (1.7V vs 2.8V). A photo of the RF-DAC based PAM-4 modulator can be seen in Fig. 4.4. The LO input signal is applied on the right side and the RF output signal is delivered at the left side of the chip. DC bias is applied on the top, while the two data input ports are located at the bottom. The total size of the MMIC including pads is  $0.55 \text{ mm}^2$ , and  $0.29 \text{ mm}^2$  without pads.

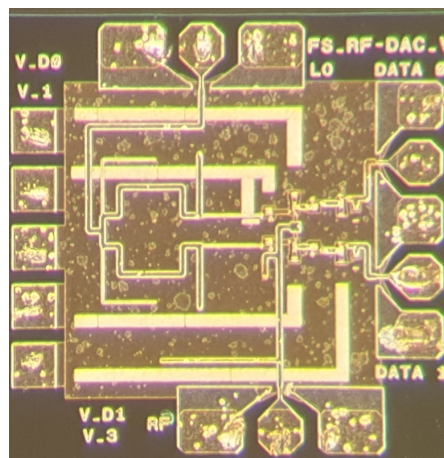


Figure 4.4: A micrograph of the fabricated RF-DAC. The chip size including pads is  $740 \mu\text{m}$  by  $740 \mu\text{m}$ .

The PAM-4 modulator was measured in frequency domain, on-wafer, using a MPI TS200 probe station. The output S21 measurement was captured with a Anritsu VectorStar ME7838A vector network analyser (VNA). A frequency sweep from 70 GHz to 130 GHz and 130 GHz to 170 GHz can be seen in Fig. 4.5. The four different traces represents the four different input data states of the PAM-4 modulator. The highest level is corresponding to data input '00', while the lowest level correspond to data input '11'. The -3dB bandwidth is between 87 GHz and 130 GHz, resulting in a 43 GHz wide band -3dB bandwidth. The difference in power between the highest power level '00' and the lowest power level '11' is approximately 10 dB for frequencies between 90-145 GHz.

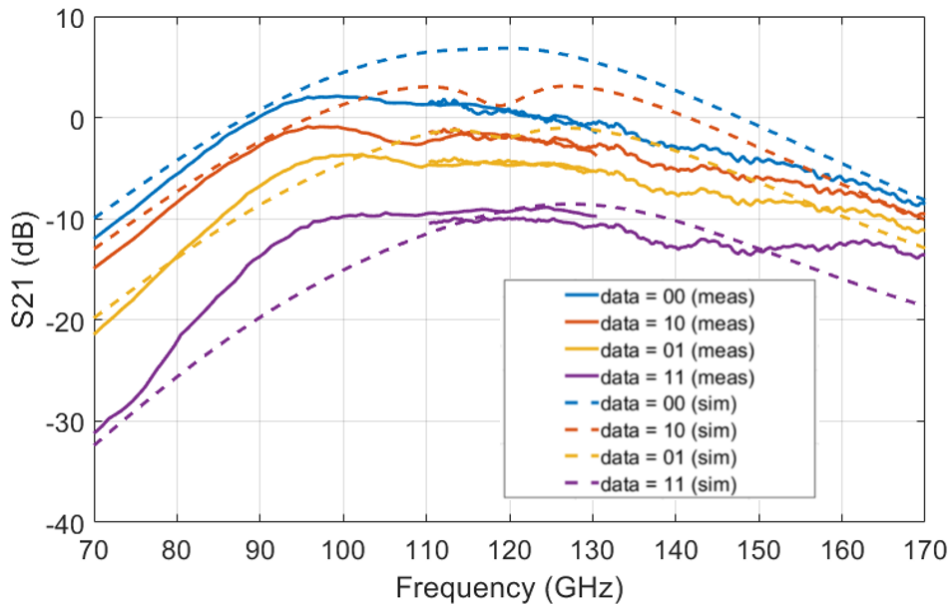


Figure 4.5: S21 for the different digital data input. LO is port 1 and RF is port 2. The measured results are shown in the solid lines and the simulated results in the dashed lines. The LO input power is -6 dBm.

#### 4.1.1 Duobinary/PAM-3 Modulator

In Paper B; three power level states were used instead of four. Three levels can be used for duobinary modulated data or PAM-3 modulated data. Duobinary modulation as an alternative modulation format of higher spectrum efficient and moderate linearity requirement, has been studied in [21].

With a binary encoder similar to that presented in [23] [24], binary input bits are coded into 3-power-level symbols that yields 1.6 bps/Hz spectrum efficiency. An RF-DAC can be used after the encoder to directly generate such PAM-3 output at desired frequency.

For PAM-3, the modulator uses three-valued logic (ternary), with three unipolar states ('0', '1', and '2'). To create these states either both data ports are "off" representing '0', one data port is "off" and one is "on" representing '1', or both data ports are "on" representing '2'.

For duobinary, the modulator also uses three states ('-1', '0', '1'). Either both data ports are "off" representing '-1', one data port is "off" and one is "on" representing '0', or both data ports are "on" representing '1'.

Applying voltage at the data input port attenuates the output signal. The voltage applied results in a corresponding attenuated output signal.

The circuit designed in this project had a bandwidth from 35 GHz to 130 GHz. A photo of the circuit can be seen in Fig. 4.6.

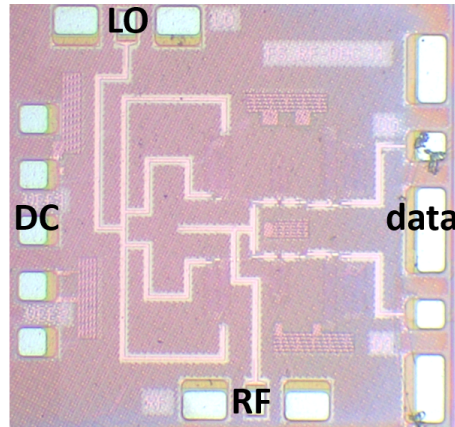


Figure 4.6: A micrograph of the Duobinary/PAM-3 modulator. The size including the pads is  $800\ \mu\text{m}$  by  $800\ \mu\text{m}$ .

The circuit was tested in time domain, using a Lecroy LabMaster 10-100Zi real-time oscilloscope to capture output RF signal, and demodulating it. PAM-3 data transmission with a bit rate of 28 Gbps was demonstrated with a symbol error rate of  $1.4 \times 10^{-6}$  (Fig. 4.7a). Using duobinary modulation data transmissions up to 30 Gbps was demonstrated with a SER of  $6.4 \times 10^{-6}$  (Fig. 4.7b).

## 4.2 Stacked RF-DAC

Another topology that was investigated is a stacked transistor design. The collector of one transistor is connected to the emitter of the other transistor, and the data is applied at one of the transistor's base, while the LO is applied at the other transistor's base. Early investigation showed that this topology has low DC power consumption.

In Fig. 4.8, there is a photograph of the first version of the stacked RF-DAC, made in the 250 nm Teledyne process and operating in E-band.

The circuit consumes 18 mW DC power, and demonstrated data rates up to 25 Gbps.

In Paper D, a new version of the stacked RF-DAC was tested, using the Infineon b11 process. A simplified schematic of the circuit can be seen in Fig. 4.9.

The circuit was designed to cover D-band and includes a frequency multiplier as well as an amplifier.

This circuit was also measured on-wafer using a probe station. The output power, for different data input, was captured with a Keysight PNA-X (67 GHz N5247A).

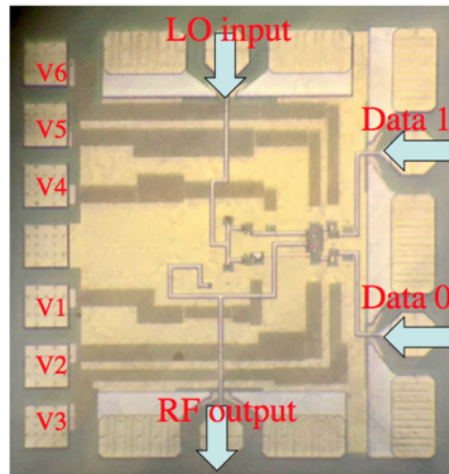
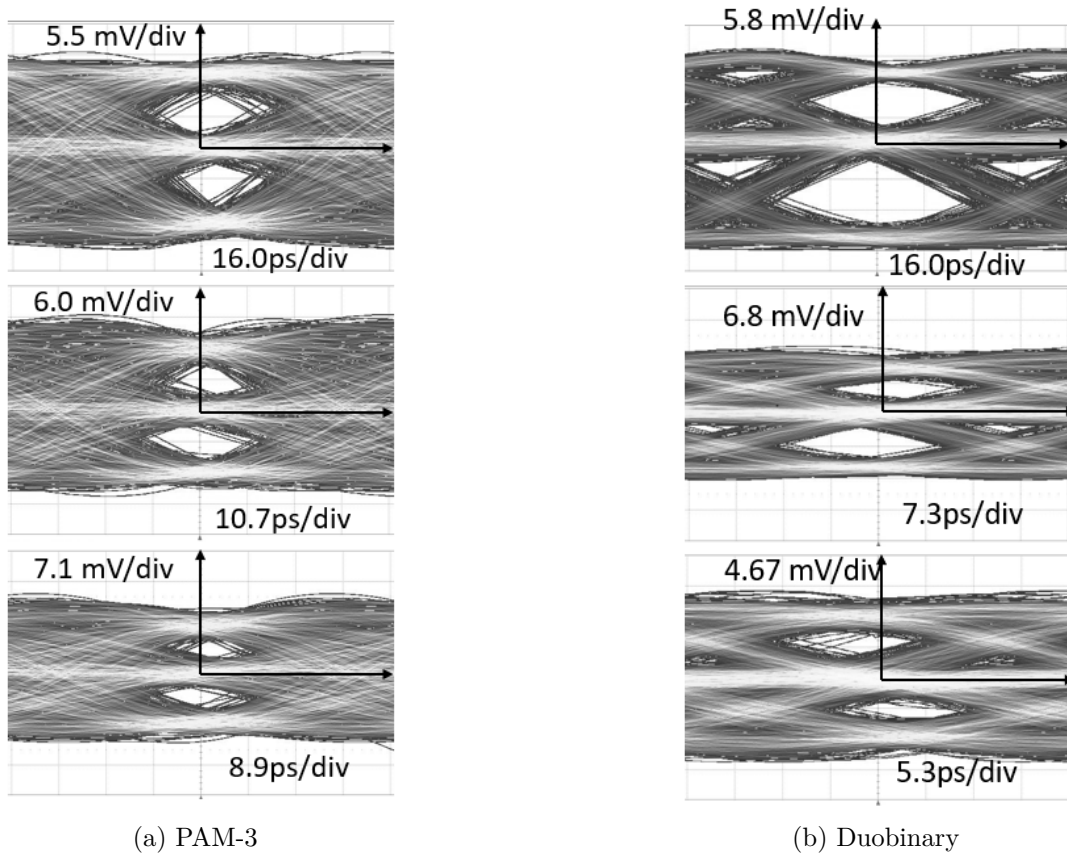


Figure 4.8: A micrograph of the stacked E-band modulator. The size including the pads is  $800\ \mu\text{m}$  by  $800\ \mu\text{m}$ .

The input power to the LO-input was 5 dBm and was swept between 55 and 85 GHz. A VDI extender WR-12 was used to provide the input signal. The output power for different data input, both simulated and measured, can be seen in Fig. 4.10.

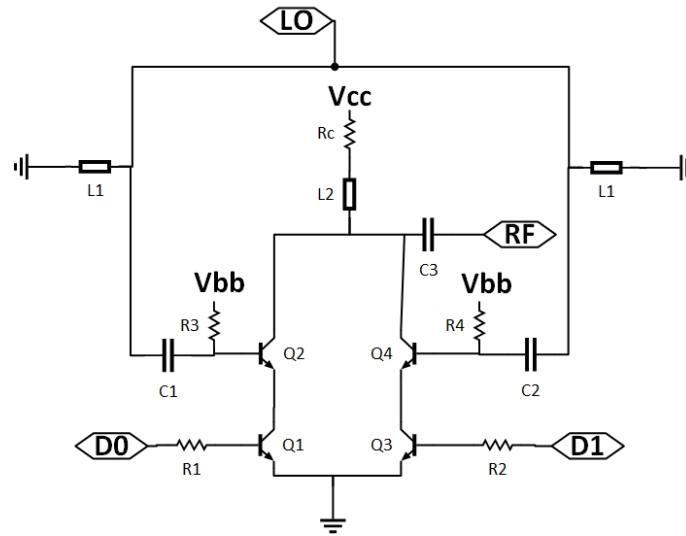


Figure 4.9: A simplified schematic of the RF-DAC

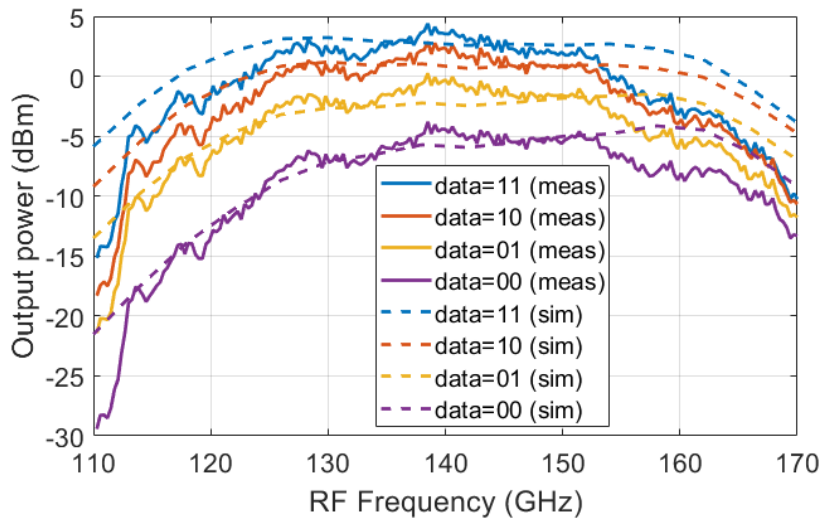


Figure 4.10: Output Power for different output frequencies at 5 dBm LO input. Solid lines represent the measurements, while the dashed lines are the simulated values.

### 4.3 Power Detectors

The receivers used for PAM in this work is based on power detectors (PD). Some of the important parameters for a PD is sensitivity, linearity and responsivity. The output voltage change should happen fast, which means that higher frequencies should have a chance to pass, while filtering out the carrier. Using a low pass filter at the output will instantly increase the response time, so it is not suitable for high data rate communication. A way to deal with suppression of the carrier is to use a balanced topology. A balun can be used to split the input signal in two, with a 180 degree phase difference (for the carrier). The leakage of the carrier will cancel each other at the output. In work by [2], both hybrids and baluns were used to suppress

different harmonics of the carrier.

In this work, PDs with a passive balun or active balun are evaluated.

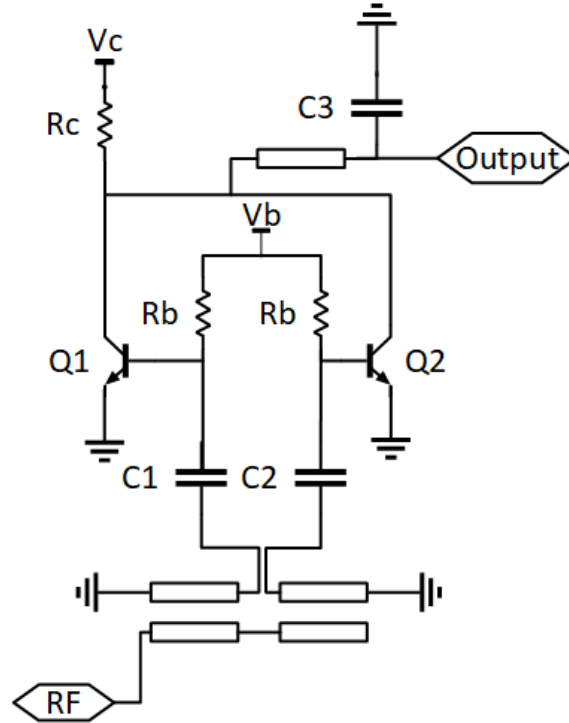


Figure 4.11: Simplified schematic of the topology used for the PD using a passive balun at the input.

The passive balun was implemented as a folded Marchand balun. The ground plane is lowered to reduce the losses. The input is on the higher level metal, which is left open at the end. The two outputs are shorted in opposite end, and are on a metal below the top input metal.

Amplifiers can be added both at the input and output depending on the requirements of the system. In Paper E this type of topology was used together with a 6-stage LNA.

The passive Marchand balun can be changed to an active solution.

As shown in Fig. 4.13, a common-emitter configured transistor, Q1, and a common-base configured transistor, Q3, are used as nonlinear components for power detectors. Their collector currents are added and applied at the stacked transistor Q4, to amplify the output signal. The output of the power detector is taken at the collector of Q4. The collector and base of Q2 are connected to form a diode which provides a DC path for Q3, and DC-bias for Q1.

The collector current of a transistor is given by a Taylor expansion

$$I_c = a_0 + a_1 V_{be} + a_2 V_{be}^2 + \dots \quad (4.1)$$

where  $a_0$  is a function of amplitude of  $V_{be}$  in an ideal case,  $V_{be}$  for common emitter configured transistor is equal to  $-V_{be}$  for common base configured transistor.

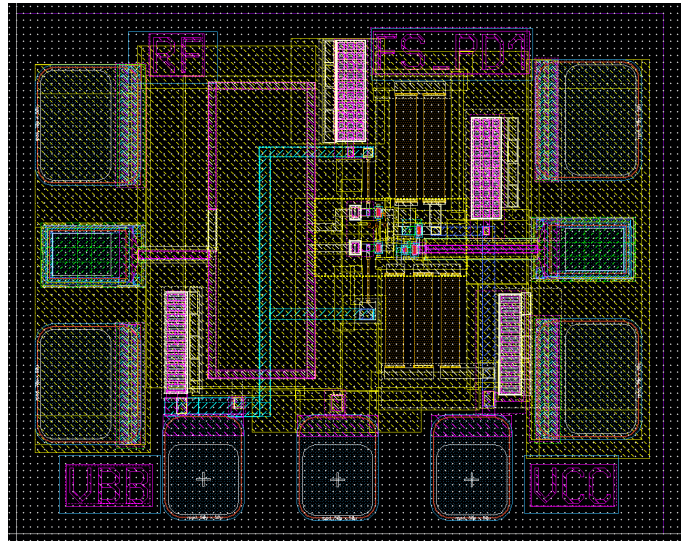


Figure 4.12: Layout of the PD with a folded Marchand balun in Infineon's B11HFC

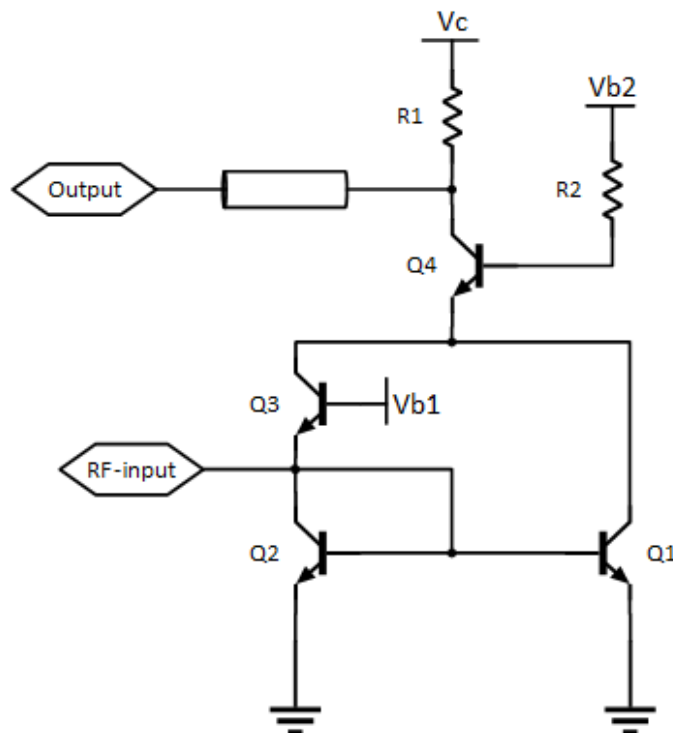


Figure 4.13: Simplified schematic of the topology used for the PD with an active balun

The single-ended input signal is applied at the base of Q1 and the emitter of Q3 simultaneously. Due to the transistor's nonlinearity, the outputs of Q1 and Q3 contain DC component and harmonics. The odd-order harmonics at the Q1 and Q3's outputs are 180 degree out of phase, since the transistor Q1 is common-emitter configured and Q3 is common-base configured. Thus, connecting Q1 and Q3's outputs, the

odd-order harmonics will be suppressed. The desired function of Q4 is amplification of the data signal, which is why a relatively large device is selected to get sufficient gain. Due to parasitic the device will have a lower gain for the RF-signal, which will help to suppress undesired fundamental and higher order harmonics.

In paper D the PD was integrated with an amplifier at the input. The fabricated PD can be seen in Fig. 4.14.

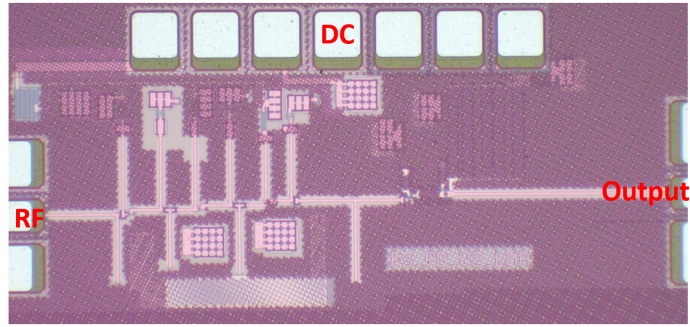


Figure 4.14: Micrograph of the PD.

The simulated output voltage in the time domain for corresponding input signal can be seen in Fig. 4.15. The carrier frequency was 130 GHz and the data rate was 20 Gbps. The simulation was done using Cadence.

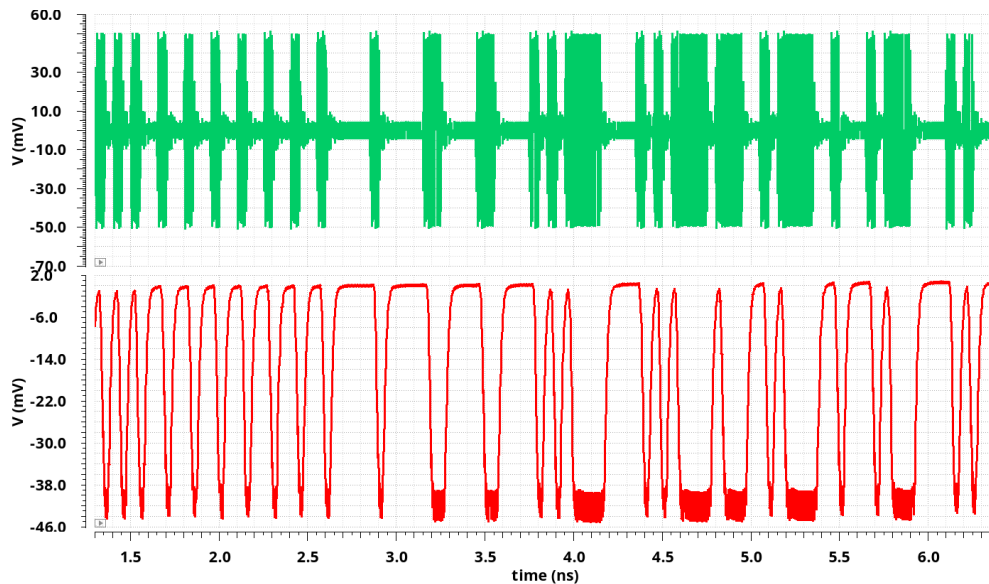


Figure 4.15: Simulated input and corresponding output from the PD, using a carrier of 130 GHz and a data rate of 20 Gbps.

The change in output voltage for different input power levels were measured. As input a D-band VDI extender WR-6.5 was used, which was calibrated using the corresponding VDI calibration kit, and verified using an Erickson power meter (PM5), VDI. The output voltage was measured using a voltage meter. The voltage change for different input powers, both simulated and measured can be seen in Fig. 4.16.

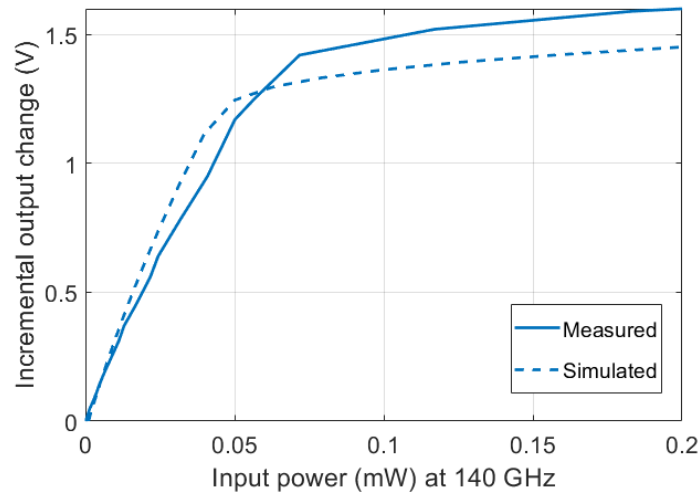


Figure 4.16: Difference in output voltage for different input powers (W). The dashed lines represent the simulated values, and the solid lines is the measured values.

The LO leakage was measured by applying 0 dBm input power, and sweeping the frequency between 110 GHz and 170 GHz. The LO isolation of the signal was measured and is displayed in Fig. 4.17.

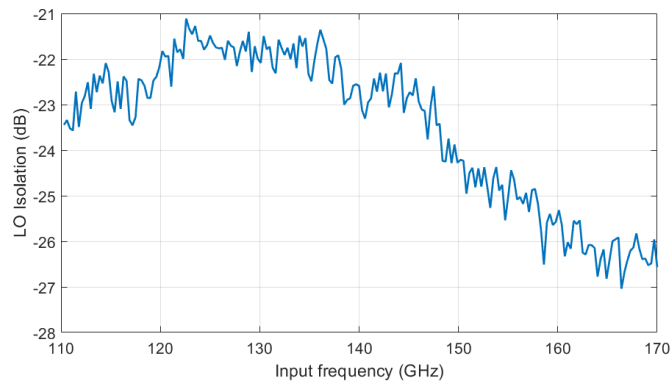


Figure 4.17: Isolation of the fundamental frequency measured at 0 dBm input power.

The DC power consumption of the PD is 59 mW, where the amplifier uses 55 mW.

## 4.4 Comparator

For a PAM-4 signal, further demodulation needs to be done to get a bit sequence out, a comparator can decide if the signal is above or below a certain voltage and give a logic answer, '0' or '1'. The reference level can be chosen according to the signal level. By using three different level a logic answer can be achieved about the

two received bits. For the highest level all outputs will be '1' corresponding to '11', the second highest level will be '110' corresponding to '10'. The third level is '100' which corresponds to '01' and the last is '000' which is then '00'. A clock signal is used to time when the signal should be read. Simulated input and output for a 10 Gbd PAM-4 signal is plotted in Fig. 4.18.

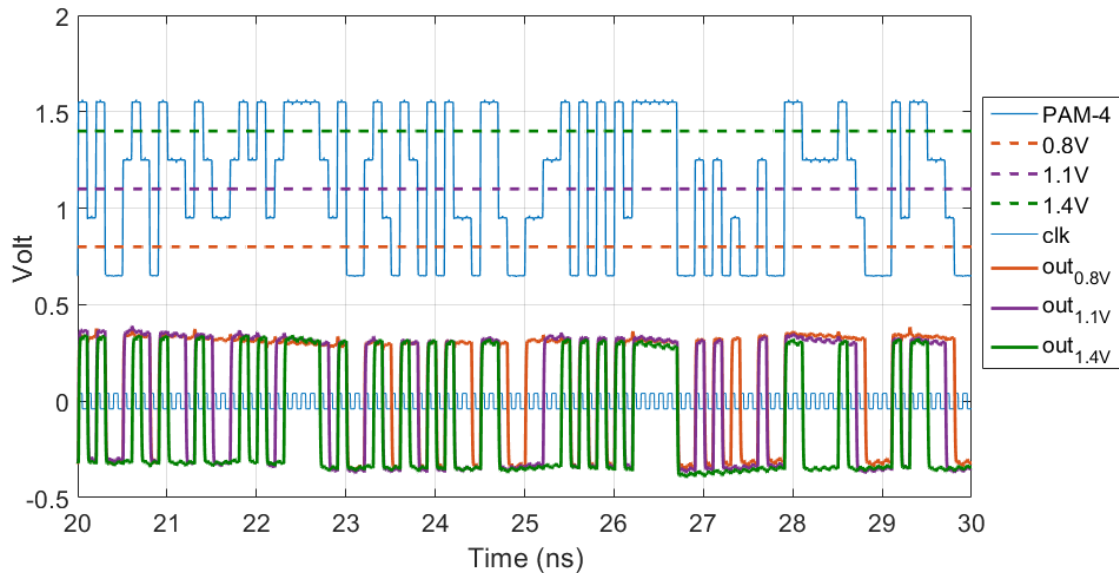


Figure 4.18: Simulated input and output for a 10 Gbd PAM-4 signal, using three different reference levels.

A design using one reference was designed and is displayed in Fig. 4.19.

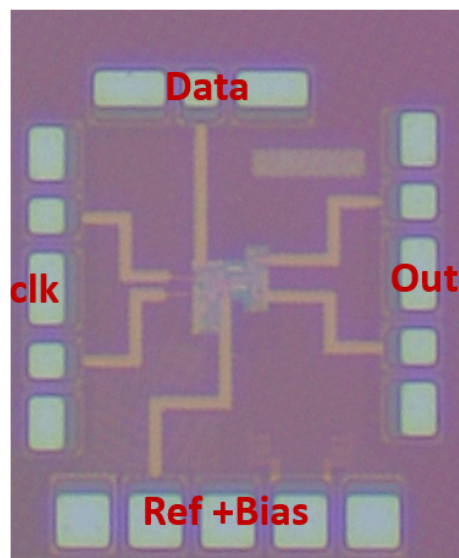


Figure 4.19: Layout for a comparator using one reference.

The circuit was measured using an AWG to create a PAM-4 data input, with a baud rate of 10 GBd. An oscilloscope was used to capture the output using three

different reference voltages, 0.8 V, 1.1 V and 1.4 V in this case. The output eye diagrams can be seen in Fig. 4.20.

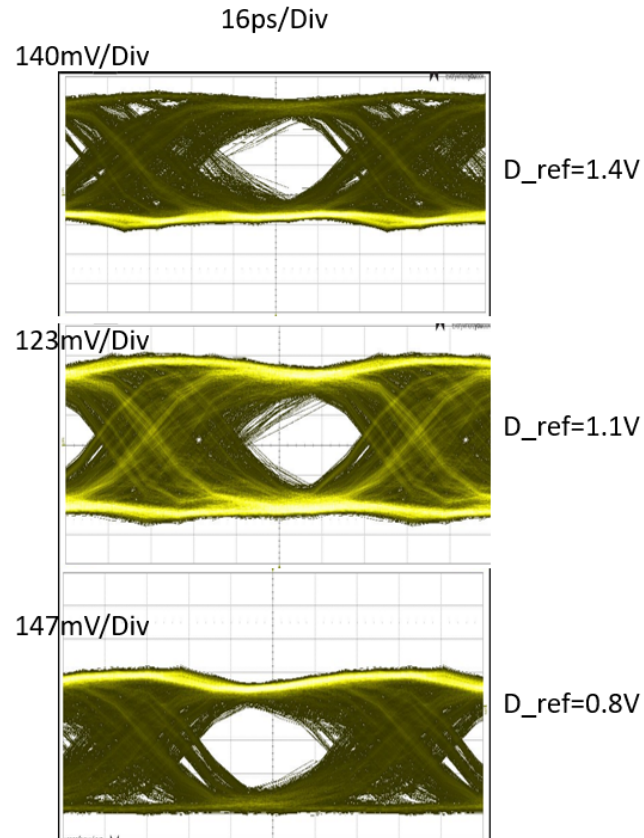


Figure 4.20: Measured eye diagram of a PAM-4 demodulated signal (10 Gbd).

By combining a PD with a comparator with three reference levels, an analog-to-digital converter (ADC) suitable for the RF-DACs discussed earlier in this chapter can be created.



## Chapter 5

# Integrated Transceivers for I/Q Modulated Communication Systems

In this chapter, integration of multi-functional high data rate I/Q modulated transmitters and receivers will be covered. The different parts included in these transceivers is presented. In Fig. 5.1 an overview of the circuits are shown in a block diagram.

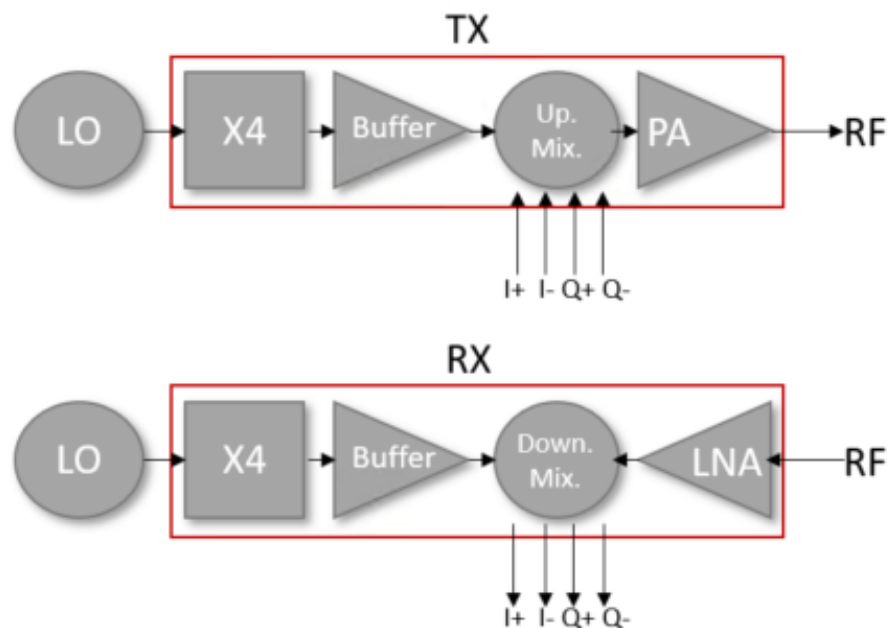


Figure 5.1: Block diagram of the transmitter and receivers designed in this thesis.

A fabricated transmitter and receiver is shown in Fig. 5.2. The total area is 3 mm by 1.448 mm for both Tx and Rx combined including pads. The Tx and Rx in this figure is used in Paper G. It is fabricated using the B11HFC and substrate thickness is 185  $\mu\text{m}$ .

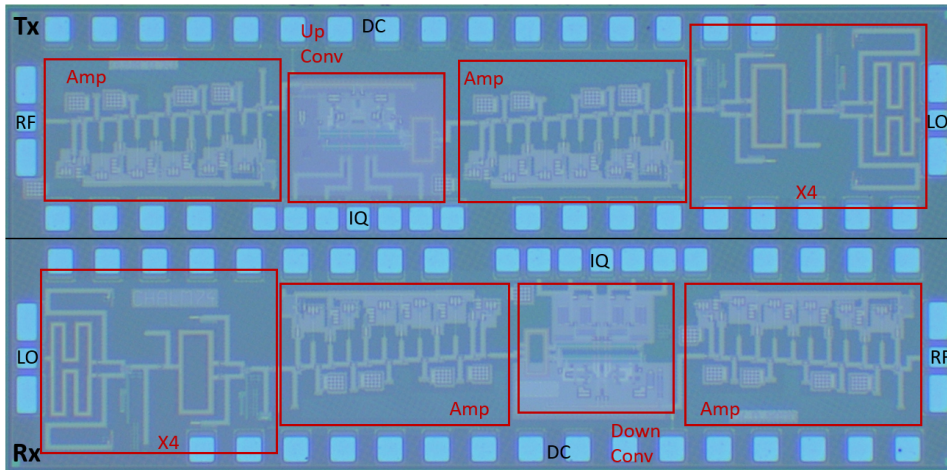


Figure 5.2: Photograph of the Tx and Rx.

## 5.1 Frequency Multipliers

Signal sources with high output power and low phase noise are challenging to find. It is increasingly harder at higher frequencies, but at the same time multiplication or amplification following an oscillator will increase the noise as well. Adding a multiplier after the signal source will increase the phase noise as  $20\log N$  dB where  $N$  is the multiplication order.

For the I/Q transceivers the signal source that was used was one fourth of the carrier frequency, because the availability of good signal sources at that frequency range is high. Frequency quadruplers had to be designed to convert the LO to the desired frequency. The quadruplers were designed using two cascaded frequency doublers. Each doubler has an emitter coupled pair which is differentially fed. The combined waveform at the collectors is rich in the second harmonic, while the fundamental tone and all odd harmonics are ideally canceled out, due to the differential input signal. The differential signal is realized using a passive Marchand balun and the transistor pair is class-B biased. The doublers in paper F used a current mirror at the coupled emitters to stabilize the current in the pair. Schematic can be seen in Fig. 5.3.

The version used in Paper G instead uses a cascoded transistor. The output from the combined collectors is fed to the emitter of a cascoded transistor to achieve higher output power. Stub matching is implemented both at input and output. Schematic can be seen in Fig. 5.4.

The suppression of unwanted harmonics is mostly created by the Marchand balun. It is challenging to design perfectly balanced baluns for a wide bandwidth.

## 5.2 Mixers

The I/Q mixers in this work is based on two double balanced Gilbert cell mixers [10]. The circuits were designed to use external DC-blocks at the I/Q ports. The LO signal is fed through an on-chip quadrature network made up by a Marchand balun

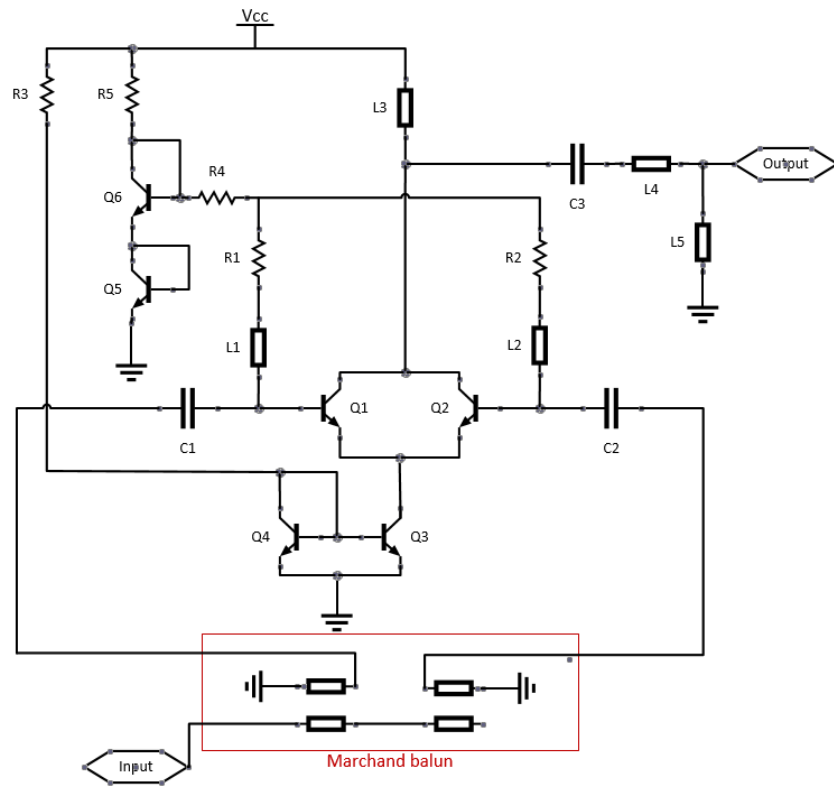


Figure 5.3: Schematic of the multiplier used in Paper F.

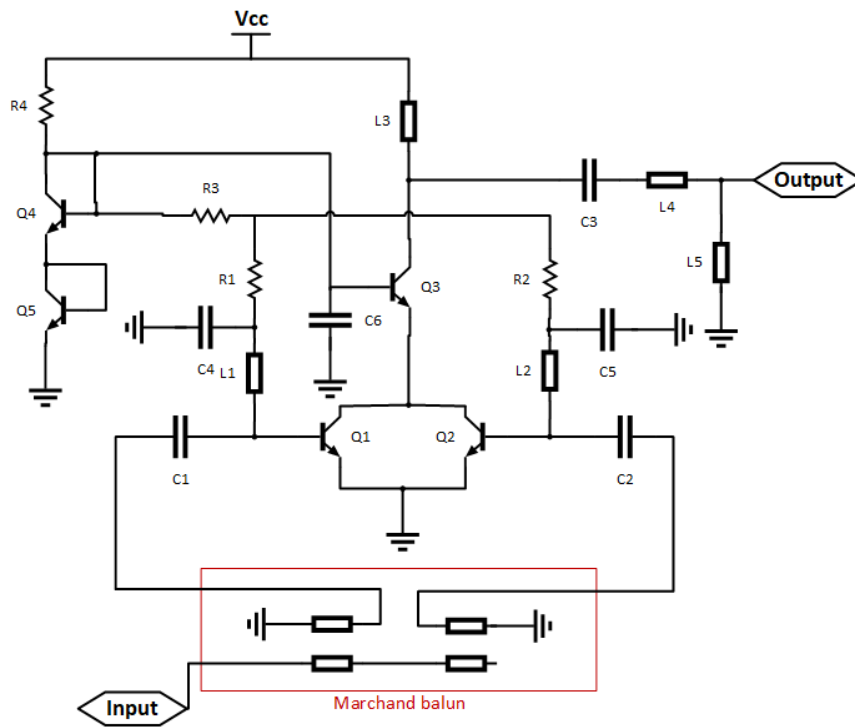


Figure 5.4: Schematic of the multiplier used in Paper G.

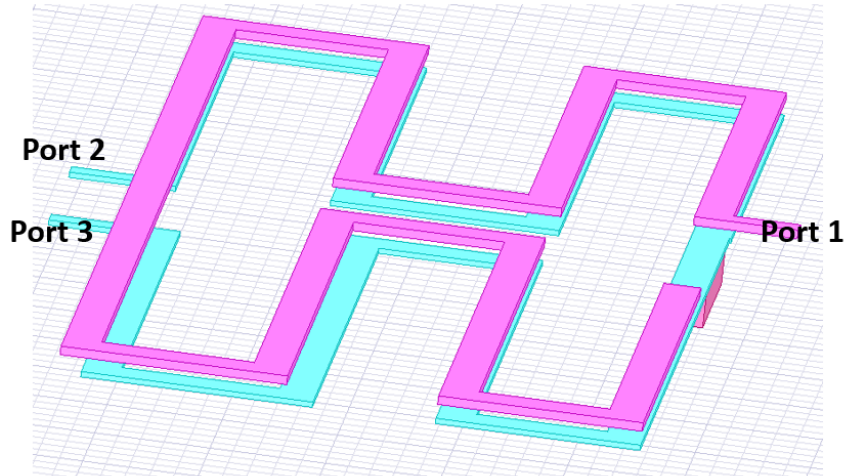


Figure 5.5: Overview of a balun designed for the E-band doubler.

and two 90 degree hybrids creating an LO with phase  $0^\circ$  and  $180^\circ$  for I channel, and an LO with  $90^\circ$  and  $270^\circ$  for Q channel. One of the Gilbert cells for the up converter mixer can be seen in Fig. 5.6. The transistor pair Q5 and Q6 work as a transconductance stage, which converts the input I/Q signals at the bases into currents at the collectors. The upper level transistors Q1-Q4 operate as switches and generate mixing products of IF and LO at the collectors, generating the RF signal. The RF outputs will be added through a Marchand balun while the LO will be canceled.

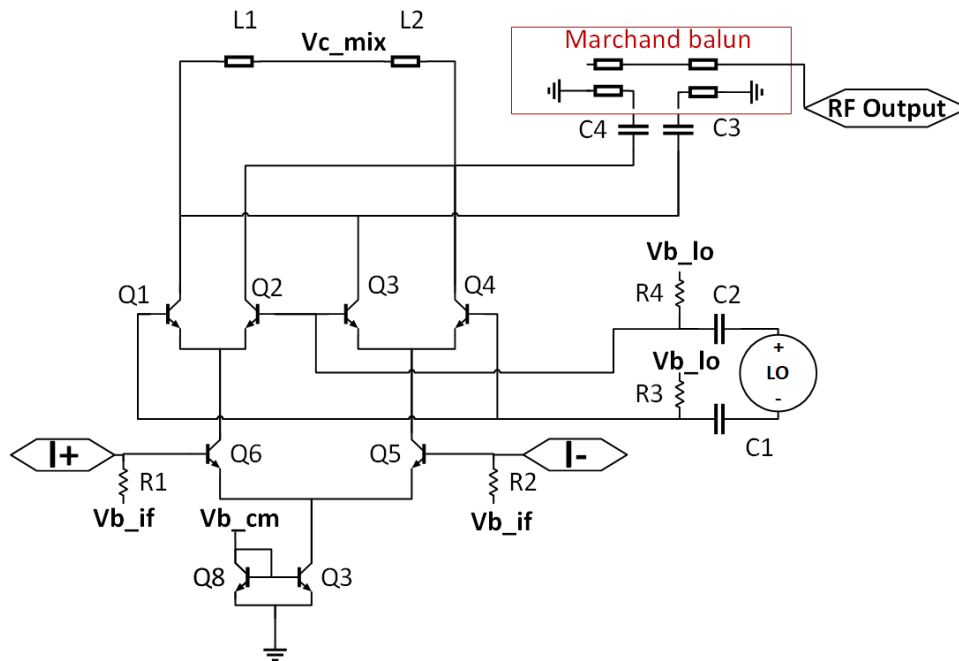


Figure 5.6: Schematic of one of the Gilbert cells of the up converter mixer.

In Fig. 5.7, the schematic of one of the Gilbert cells for the down converter mixer

is shown.

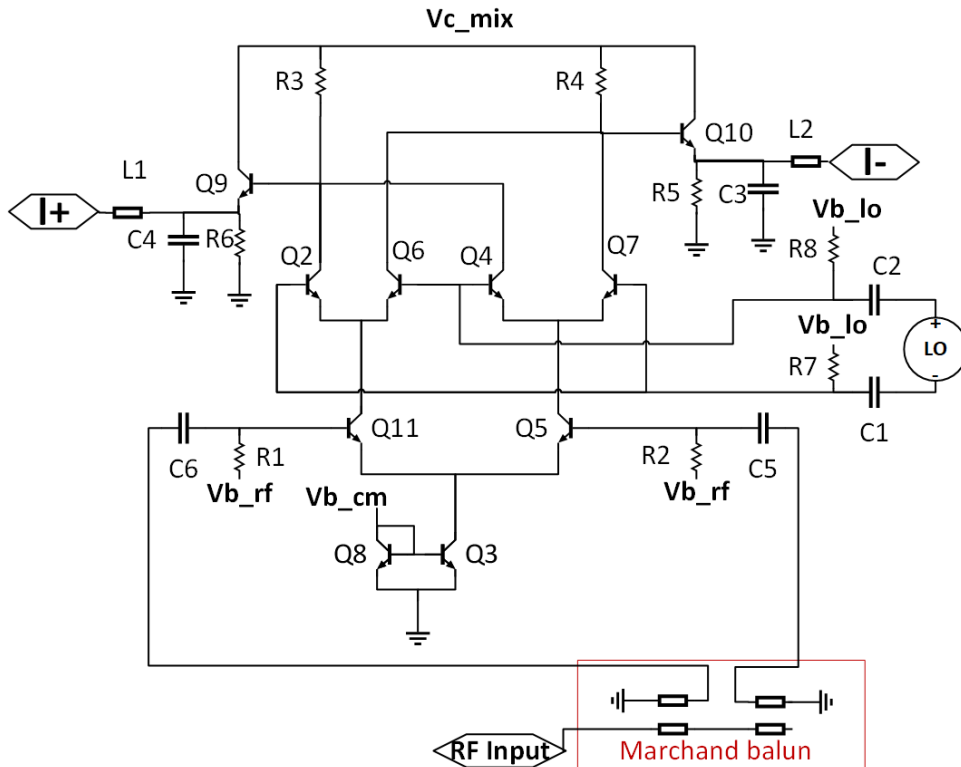


Figure 5.7: Schematic of one of the Gilbert cells of the down converter mixer.

### 5.3 Amplifiers

Two different topologies were used. The first one is a multistage common emitter amplifier. The amplifier has high pass interstage matching to achieve flat, wideband gain. Versions with three and six stages were implemented. For the power amplifier (PA) versions the transistor size increased at each stage, while the low noise amplifier (LNA) version kept the same size. The schematic is displayed in Fig. 5.8.

A balanced cascoded version was also used in some of the integrations (for example Paper H), and the schematic is displayed in Fig. 5.9. The benefit of using a balanced design is that the quality of the grounding of the circuit is not as crucial as well as a higher output power.

### 5.4 Integrated Tx and Rx Challenges

In Paper F the first version of the integrated circuits were evaluated. The conversion gain for the transmitter/receiver was measured with an input IF/RF power of -15 dBm as well as an LO power at feed into the quadrupler of 8 dBm. The IF was fixed at 2 GHz and both the lower sideband (LSB) and the upper sideband (USB)

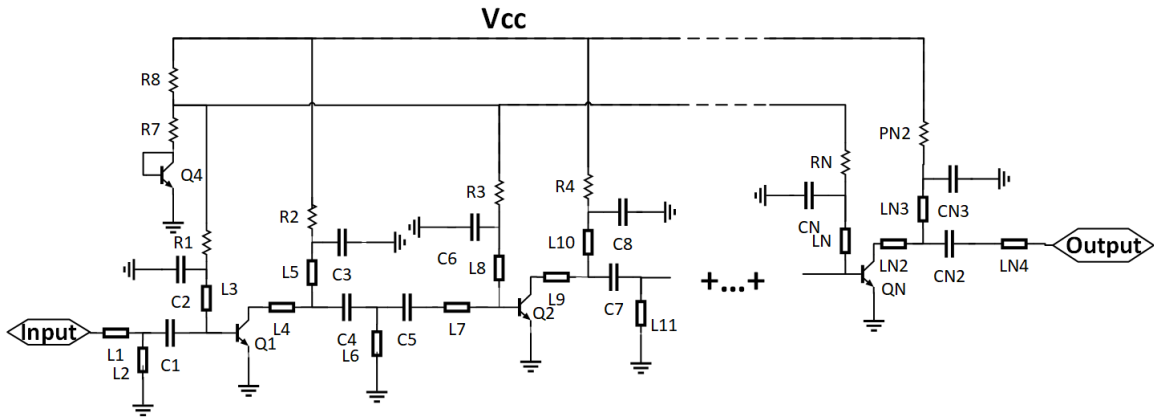


Figure 5.8: Schematic of the common emitter amplifier.

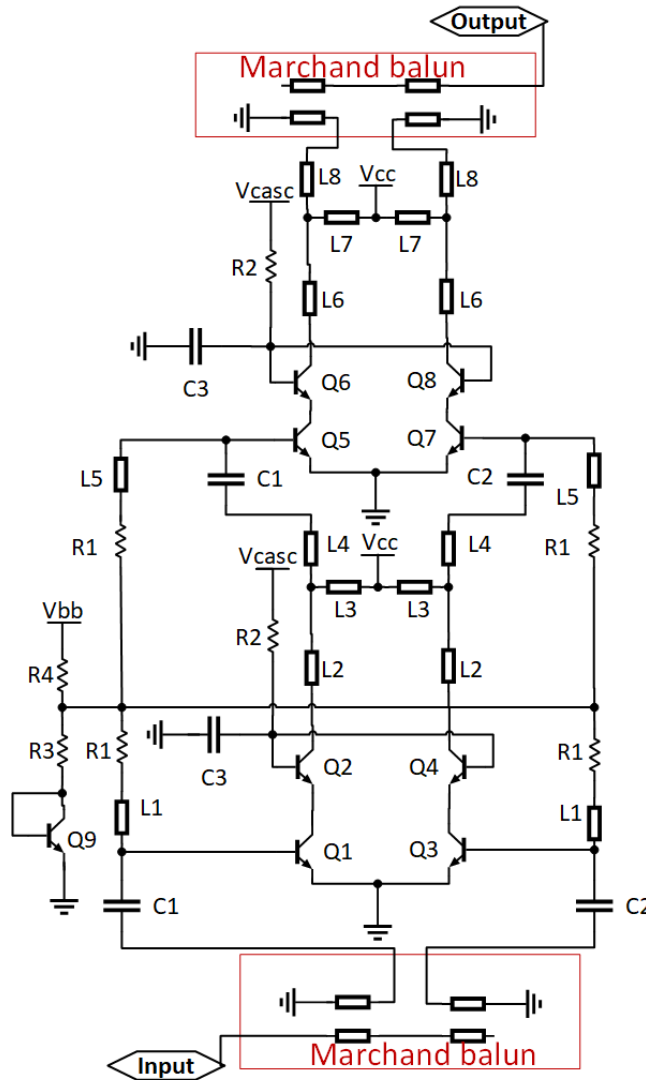


Figure 5.9: Schematic of the balanced amplifier.

was measured sweeping the RF frequency. The IF input/output was split into four channels using an external balun and two hybrids. The measurement result can be seen in Fig. 5.10 and Fig. 5.11.

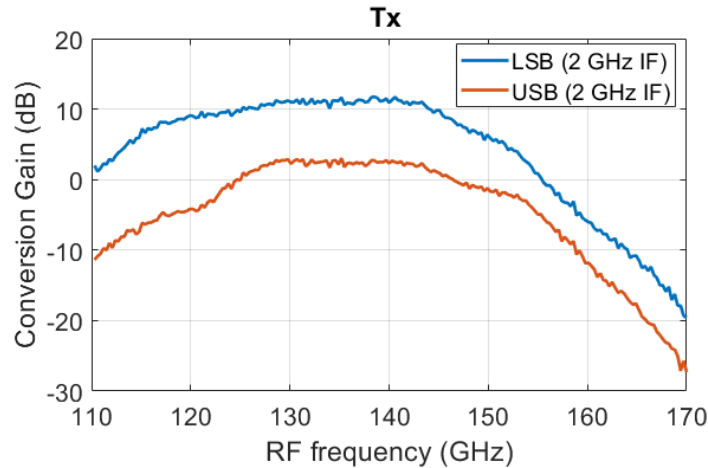


Figure 5.10: Conversion gain for an RF sweep with a 2 GHz IF.

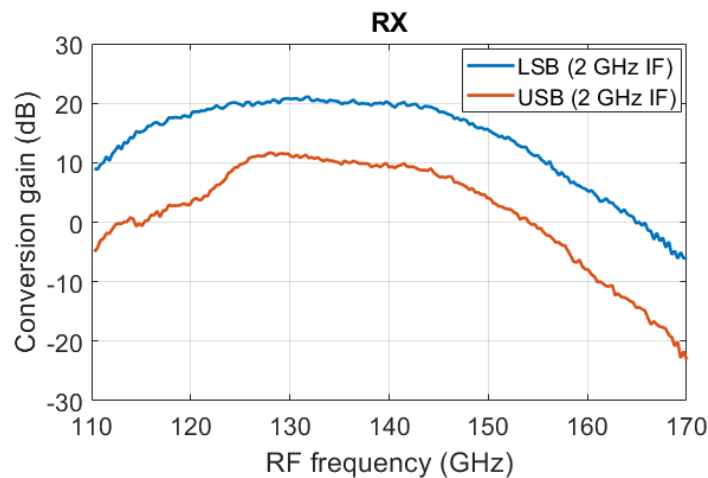


Figure 5.11: Conversion gain for an RF sweep with a 2 GHz IF.

These circuits together formed a link that demonstrated 40 Gbps QAM-16 data transmission, with a BER of  $= 9.8 * 10^{-5}$  and 20 Gbps QPSK with  $BER < 10^{-12}$ . The link required a fairly high LO power and an IF had to be used to modulate the signal.

The development to increase data rate from the version in Paper F focused on covering the higher parts of D-band, increase the sideband suppression, and reducing the amount of LO power required to drive the circuits. The result is the circuits in Paper G. The LO input power was decreased to 4 dBm and the bandwidth was increased from 30 GHz to 40 GHz. Sideband suppression was also increased allowing for direct modulation to be used. The sacrifice was the peak output power that went from 3 dBm to 0 dBm. Conversion gain for these circuits can be seen in Fig. 5.12

and Fig. 5.13. Note that different IF frequencies were used compared to the first version.

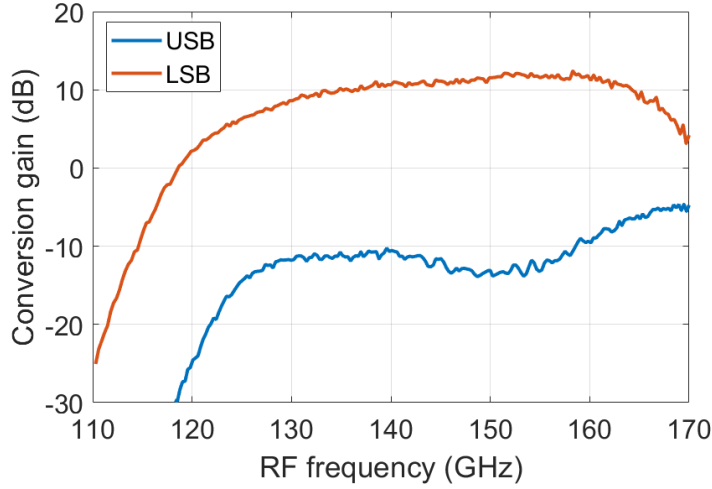


Figure 5.12: Measured conversion gain for the Tx using a 4 GHz IF signal.

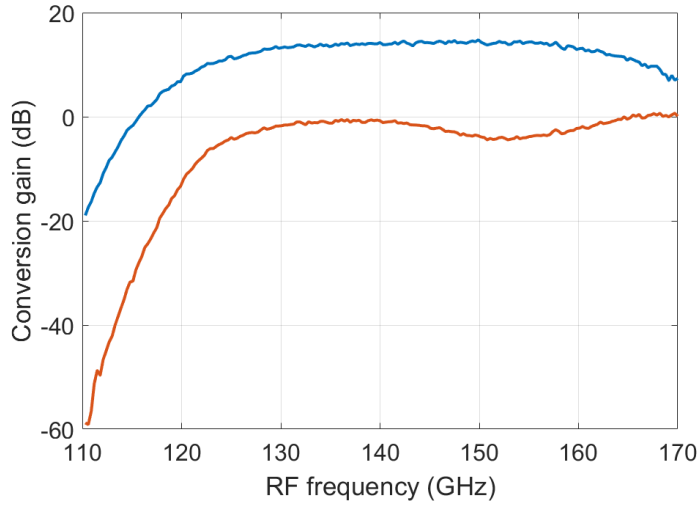


Figure 5.13: Measured conversion gain for the Rx using a 4 GHz IF signal.

As can be seen from the Fig. 5.12, a typical conversion gain of around 10 dB was measured between 125 - 165 GHz, and a sideband suppression of  $\approx 20$  dB was achieved. The highest sideband suppression (25 dB) was around 152 GHz.

Sideband suppression is a result of I/Q (im-)balance. Amplitude error and phase error will limit the signal-to-distortion ratio (SDR). SDR is given by;

$$\text{SDR} = 10\log\left(\frac{1 + \epsilon_R^2 + \epsilon_R^2 \tan^2(\Delta\phi_R)}{\epsilon_R^2 + \tan^2(\Delta\phi_R)}\right) \quad (5.1)$$

where  $\epsilon_R$  is the amplitude error and  $\Delta\phi_R$  is the phase error. For an SDR above 20 dB the phase error has to be lower than 6 degrees or the amplitude error less than

10 % [14]. Known distortion can be dealt with, but it is increasingly difficult to do at high data rates, in real-time, which is why it can be seen as noise in those cases.

Captured waveforms when only I/Q channel is used and both channels are used can be seen in Fig. 5.14. 10 Gbd QPSK modulated data was used and a carrier of 151 GHz. In the first case the input to the Q channel was turned off, second case I channel was turned off.

Some leakage between the channels (cross-talk) can be seen in Fig. 5.14. The cross-talk will limit the SNR and stay fairly constant independent of the signal's bandwidth.

The output spectrum from the Rx for different data rates of QPSK modulated signals was measured and can be seen in Fig. 5.15, making sure that the signal was strong enough compared to the noise floor.

LO leakage is also a concern which is why the output spectrum of a modulated 5 Gbd QPSK signal from Tx was measured by a Rohde & Schwarz Signal Source Analyzer (FSUP50) via an external signal analyzer mixer (SAM-170). The output spectrum is displayed in Fig. 5.16.

By adding a bias tee to the I+ and Q+ port a small voltage change (a few mV) could significantly improve the LO leakage. Fig. 5.17 shows the output spectrum of a 5 GHz continuous wave (CW), with 90 degree offset between channels to show sideband suppression, where the one on the left is without bias tee, and the one on the right is with bias tee.

Another challenge for high frequencies, recently explored in high-data rate communication is that it has been demonstrated that the modulation order is limited by far-carrier LO noise floor [1] [17].

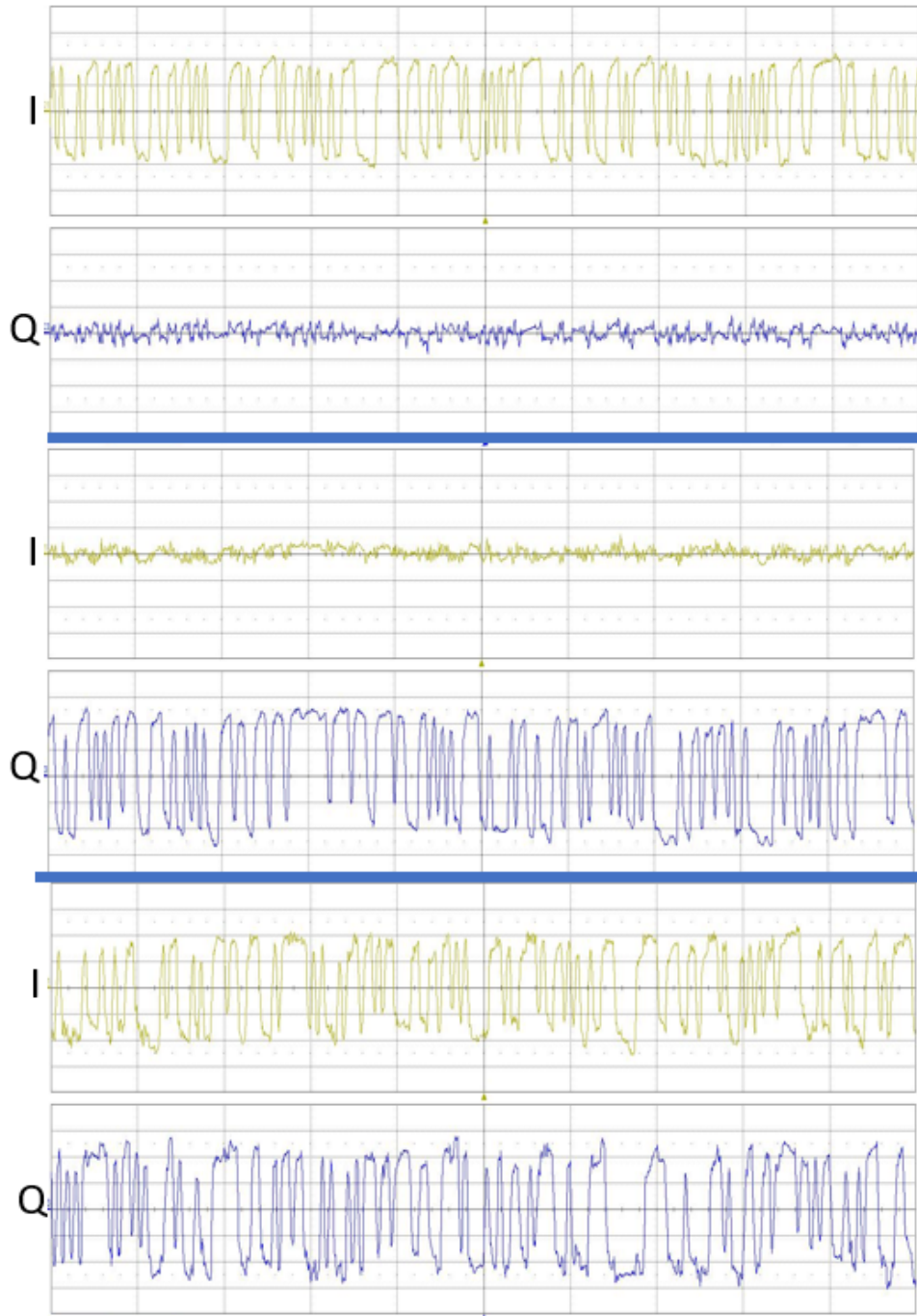


Figure 5.14: Output waveform from the oscilloscope when data is only transmitted from one channel at a time in the first two cases. On top only the I channel is used, in the middle only Q channel is used, and at the bottom both channels are used. The symbolrate was 10 Gbd with a carrier of 151 GHz.

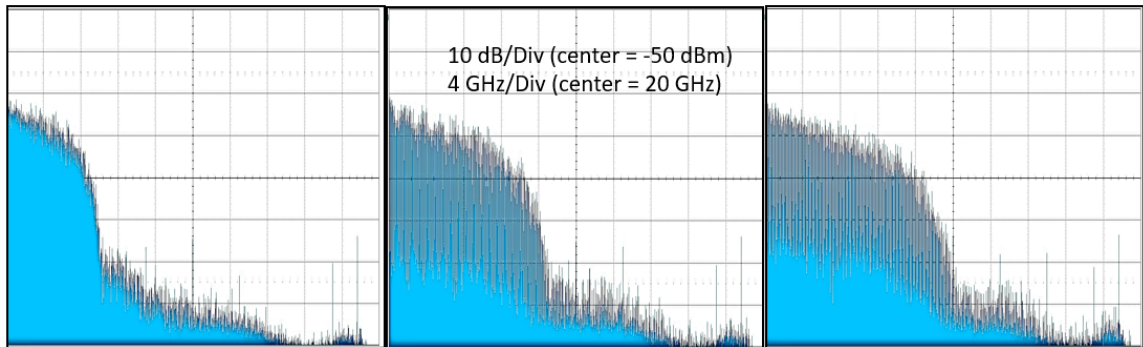


Figure 5.15: Spectrum of a QPSK modulated signal received by the oscilloscope from the Rx. From the left 15 Gbd, center 25 Gbd and the right 30 Gbd. (LO = 151 GHz)

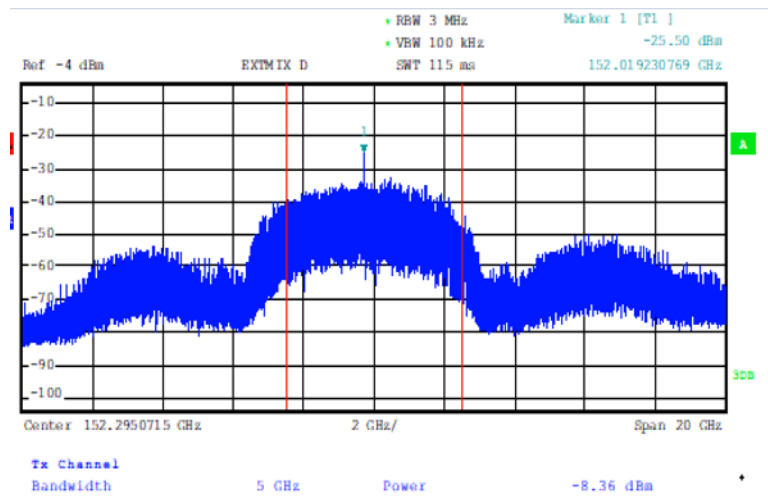


Figure 5.16: 5 Gbd QPSK with LO at 152 GHz.

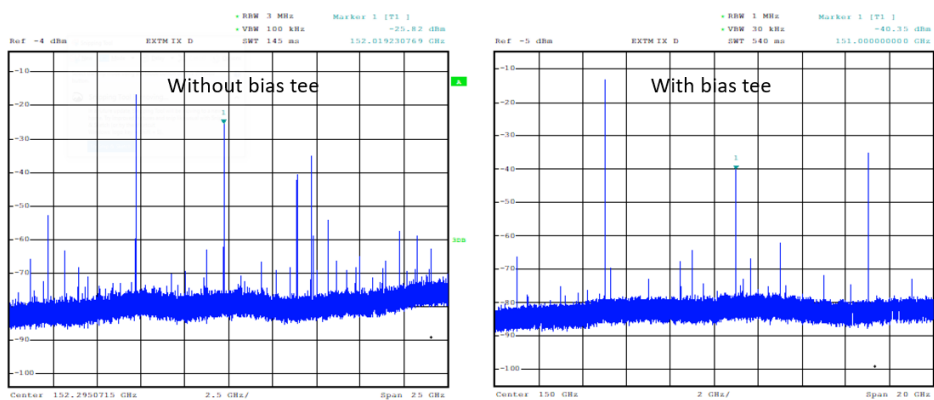


Figure 5.17: 5 GHz CW with LO at 152 GHz with and without bias tee at the I+ and Q+ port.



# Chapter 6

## Evaluation of the Communication Systems

In Paper C, Paper D, Paper E, Paper F, Paper G and Paper H transmitters and receivers were tested together during real-time link measurements. The links were measured using two probe stations, one for transmitter and one for receiver.

### 6.1 PAM Modulated Tx/Rx in 250 nm InP DHBT Technology

The F-band "emitter coupled pair"-based RF-DAC (section 4.4) was used as a transmitter in the link. The PD receiver used an active balun at the input. A photo of the PD can be seen in 6.1.

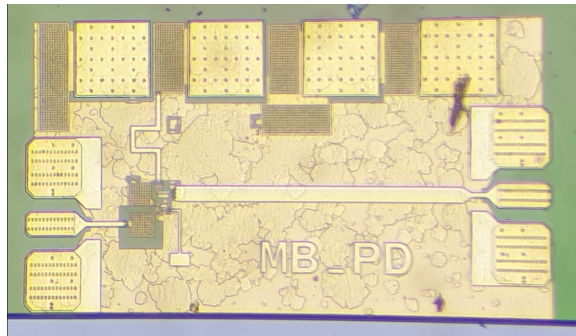


Figure 6.1: The PD used during the link measurements. The chip size including pads is  $700 \mu\text{m}$  by  $400 \mu\text{m}$ . Courtesy: Mingquan Bao

The link was tested in time domain transferring data in real time. The one meter PMF from Lehrstuhl für Hochfrequenztechnik (LHFT), University of Erlangen, Germany, was used to connect the circuits.

The output from the PD was connected using coaxial cable to a Lecroy Lab-Master 10-100Zi real-time oscilloscope where the signal could be analyzed. A photo of the fiber connecting the circuits on each probe station can be seen in Fig. 6.2.

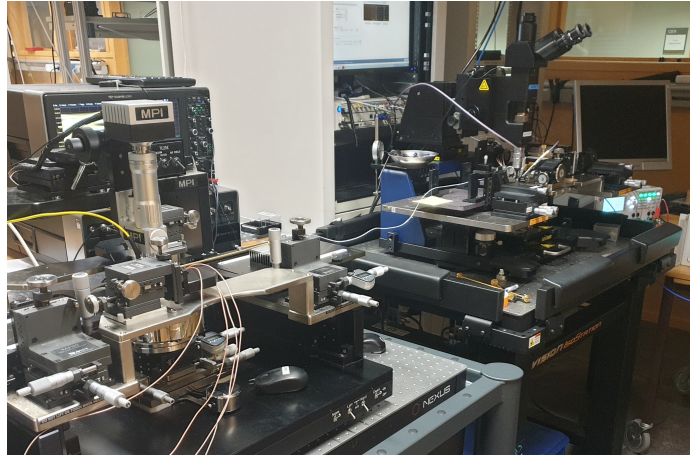


Figure 6.2: The setup that was used in the PMF link measurements. The fiber can be seen connecting one circuit on one probe station to the other one on the other probe station.

The LO input signal for the RF-DAC was provided by a Keysight signal generator (Agilent 67 GHz PSG E8257D) through an VDI extender WR 6.5. The LO input frequency was set to 130.6 GHz, which together with the probe loss results in an input power of approximately -1.5 dBm delivered at the input of the RF-DAC. The data input was provided by a Keysight M8195A arbitrary waveform generator (AWG).

First, the PMF link was tested using only one data input (MSB) to create a PAM-2 modulated signal. Bit rates up to 32 Gbps was measured and the data input that was used was a PRBS-9 stream. The eye diagram of the output signal from the PD can be seen in Fig. 6.3 (a) for a 30 Gbps signal and in Fig. 6.3 (b) for a 32 Gbps signal. For a 32 Gbps signal the bit error rate (BER) was  $2.6 \times 10^{-10}$ .

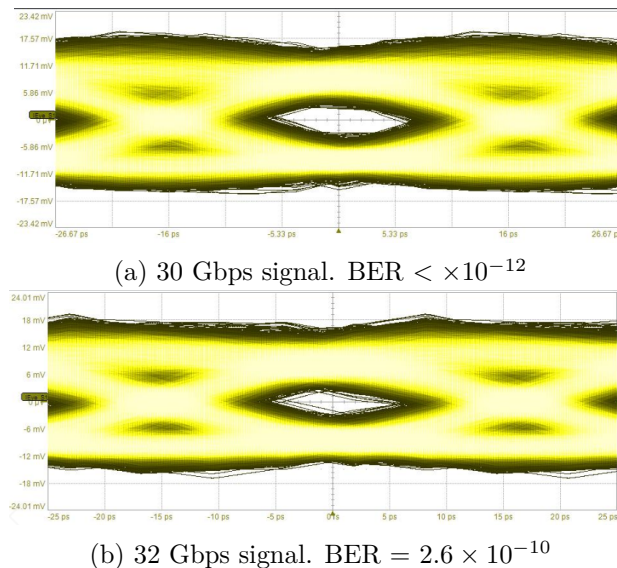


Figure 6.3: Eye diagrams from the demodulated PAM-2 signal at 130.6 GHz.

For the PAM-4 PMF link measurements, a PRBS-9 stream was used at the MSB data port and a PRBS-10 stream was used at the LSB data port. Data rates up to

15 GBaud were tested, corresponding to 30 Gbps. For 30 Gbps PAM-4 transmission the BER was  $4.3 \times 10^{-10}$ . Eye diagrams of the measurements can be seen in Fig. 6.4.

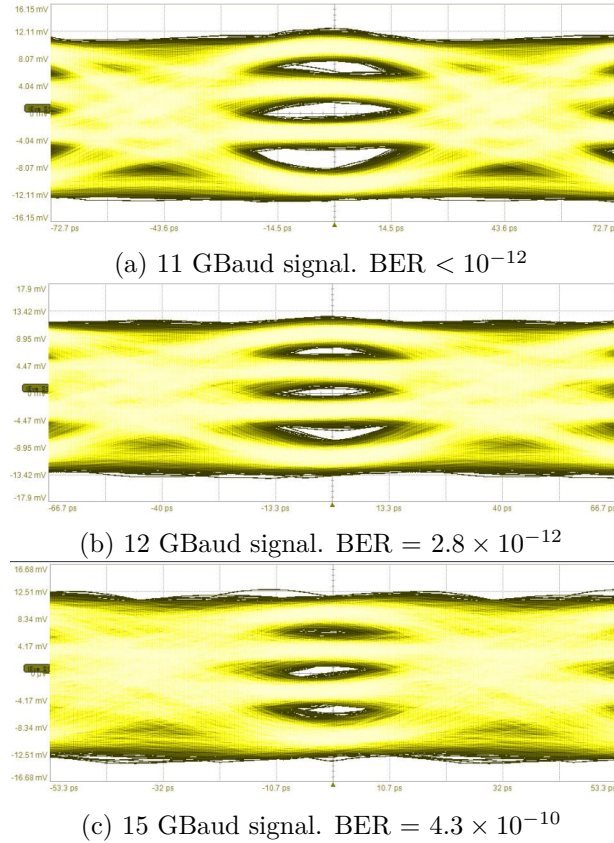


Figure 6.4: Eye diagrams from the demodulated PAM-4 signal.

The total DC power consumption for the PMF link was measured to be 123 mW, which results in an energy efficiency of 4.1 pJ/bit for a 30 Gbps data transmission.

## 6.2 PAM Modulated Tx/Rx in 130 nm SiGe BiCMOS Technology

The parallel stacked RF-DAC was used as a transmitter. It included a frequency multiplier at the LO input and an amplifier at the output. A block diagram of the RF-DAC can be seen in 6.5.

The fabricated RF-DAC is depicted in Fig. 6.6. The circuit is supplied by two DC biases of 2 V and 3 V. The circuit size is  $1.18 \times 0.72 \text{ mm}^2$ , including pads. A signal generator (PSG 20 GHz Agilent E8257D) provided the LO input signal for the RF-DAC

The same PMF, oscilloscope and AWG as in the previous link measurement were used in this measurement. A photo of the fiber connecting the circuits on each probe station can be seen in Fig. 6.7.

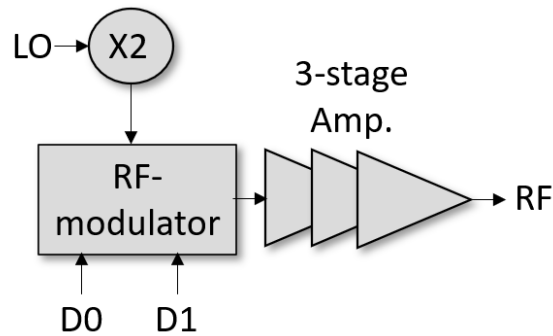


Figure 6.5: Block diagram of the RF-DAC.

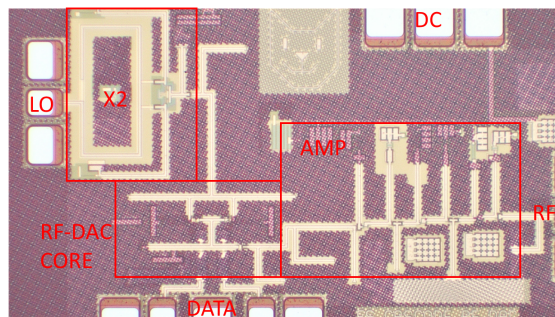


Figure 6.6: Photograph of the RF-DAC.

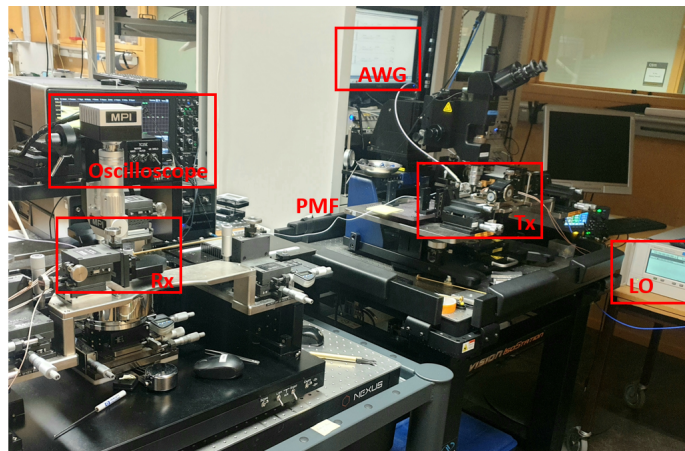


Figure 6.7: Setup that was used during the link measurement.

The LO input signal for the RF-DAC was provided by a signal generator (PSG 20 GHz Agilent E8257D) through a VDI extender WR-12. The LO input frequency was set to 69 GHz, resulting in a center RF-frequency of 138 GHz. Two pseudorandom binary sequences (PRBS-9 and PRBS-10) were provided by the AWG to generate the data. Different combinations of pulse shaping of the input stream, by the AWG, and equalization of the output stream, by the oscilloscope, were used. The equalizer is a Finite Impulse Response (FIR) equalizer, using 21 taps [30]. An external DC block was used at the output of the PD during all measurements.

In Fig. 6.8 eye diagrams of the output can be seen, using a carrier frequency

of 138 GHz. Figure 6.8 A, both root-raised cosine (RRC) pulse shaping, with a roll-off factor of 1, and de-emphasis (DE) with one -5 dB post-cursor tap was used. Equalization (FIR with 21 taps) is used at the output. Figure B uses the same pulse shaping as Figure A, but without equalization at the output. Figure C uses no pulse shaping of the input bit stream, but equalization at the output of the PD. Datarates are 10 Gbaud (20 Gbps), 9 Gbaud (18 Gbps) and 8 Gbaud (16 Gbps), and the bit error rate (BER) of the transmissions are less than  $10^{-12}$ .

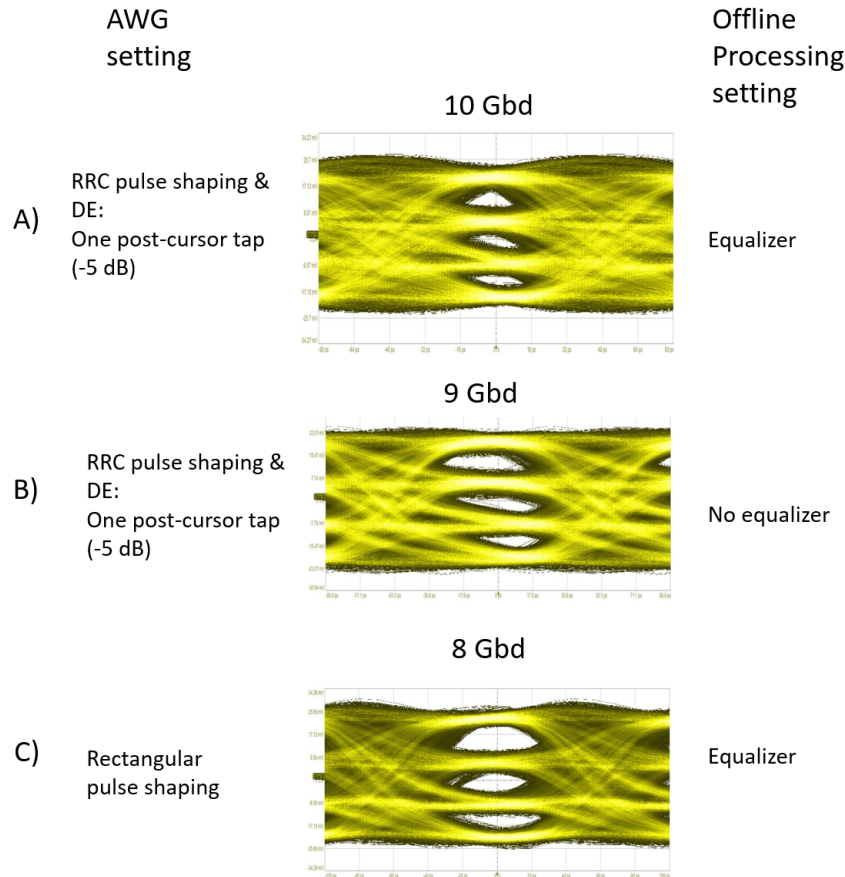


Figure 6.8: Eye diagrams of the output from the PD at 69 GHz LO (138 GHz RF) for A) 10 Gbaud using RRC pulse shaping and DE with one -5 dB post-cursor tap. Equalization is also used at the output. B) 9 Gbaud using RRC pulse shaping and DE with one -5 dB post-cursor tap. C) 8 Gbaud with no pulse shaping, but equalization is used at the output. All transmissions have a BER  $< 10^{-12}$ .

In Fig. 6.9, eye diagrams for baud rates between 6 Gbaud and 4 Gbaud, corresponding to 12 Gbps and 8 Gbps, are shown. No equalization was used at the output of the PD, and all transmissions have a BER  $< 10^{-12}$ . In Figure D, de-emphasis with one -5 dB post-cursor tap is used, while in Figure E, de-emphasis with one -3 dB post-cursor tap is used. In Figure F, RRC pulse shaping with a roll-off factor of 1 is used. In Figure G, no pulse shaping (rectangular) is used of the input bit stream. It is shown that pulse shaping and/or equalization can be used with benefit to counteract the dispersive effects of the fiber.

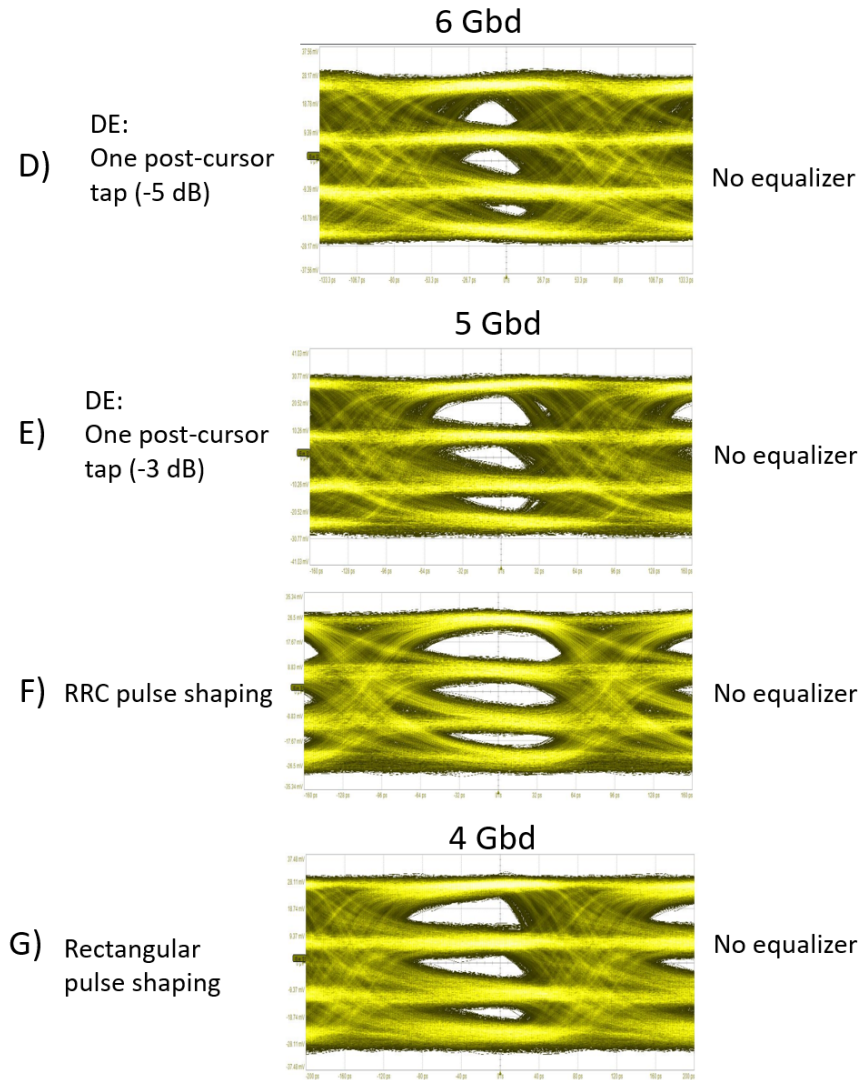


Figure 6.9: Eye diagrams of the output from the PD at 69 GHz LO (138 GHz RF) for D) 6 Gbaud using DE with one -5 dB post-cursor tap. E) 5 Gbaud using DE with one -3 dB post-cursor tap. F) 5 Gbaud using RRC pulse shaping. G) 4 Gbaud with no pulse shaping. All transmissions have a BER  $< 10^{-12}$ .

### 6.3 I/Q Modulated Tx/Rx in 130 nm SiGe BiCMOS Technology

A two probe station setup was also used for the multi-functional I/Q modulated transmitter and receiver. In this case the LO was provided by a Keysight signal generator (Agilent 67 GHz PSG E8257D), which was shared by Tx and Rx using a power splitter. The AWG provided a differential I/Q signal using root raised cosine pulse shaping with a roll off of 0.7. Differential I/Q was measured by the oscilloscope from the Rx. An overview of the setup can be seen in Fig. 6.10.

A one meter foam-cladded PMF provided by Huber+Suhner was used and can be seen connecting the Tx and Rx in Fig. 6.11. DC blocks were added on the I/Q

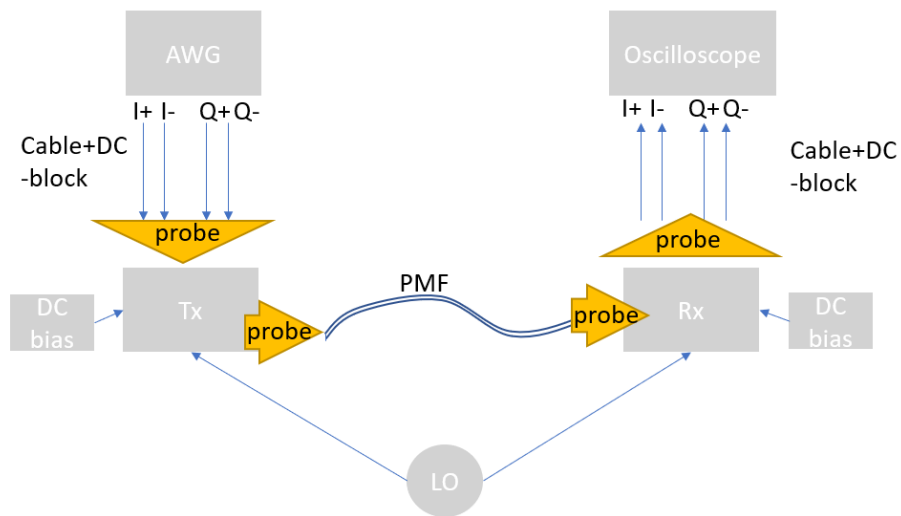


Figure 6.10: Simple sketch of the measurement setup.

ports both on receiver and transmitter, and the probe configuration was GSSGSSG.

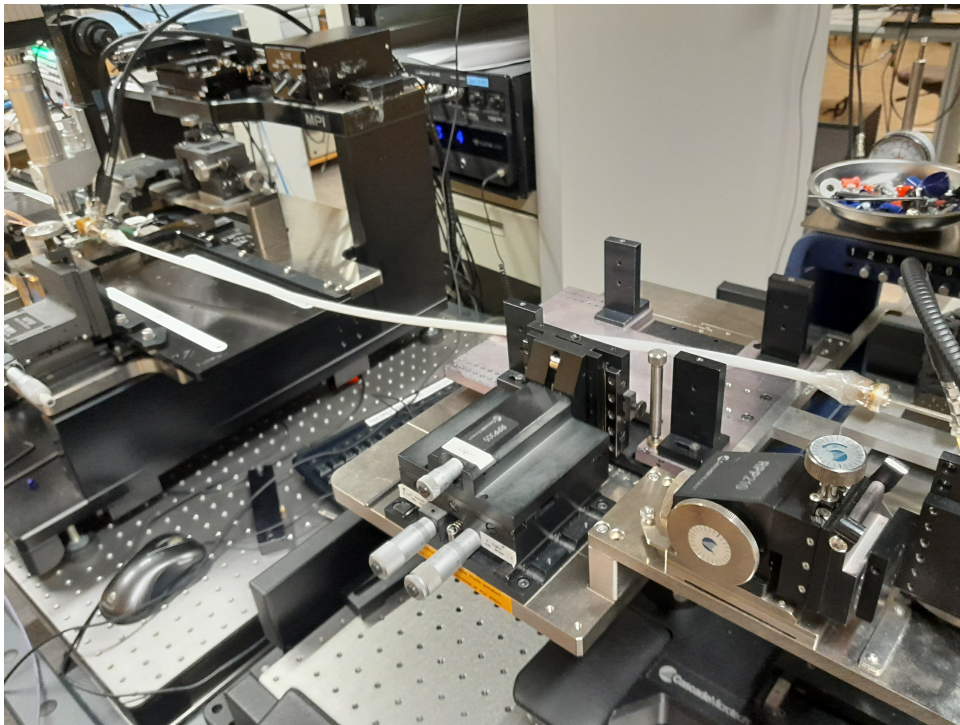


Figure 6.11: The setup that was used during the link measurements.

The captured signals from the I/Q- ports were subtracted from the I/Q+ signals to increase signal strength. The bandwidth of the oscilloscope is 36 GHz. No filter was used, but the signal was equalized to counteract the dispersive effects from the fiber and the cables. The equalizer is a Finite Impulse Response (FIR) equalizer, using 27 taps. Captured eye diagram and IQ constellation for a 28 GBd QPSK modulation can be seen in Fig. 6.12, corresponding to 56 Gbps.

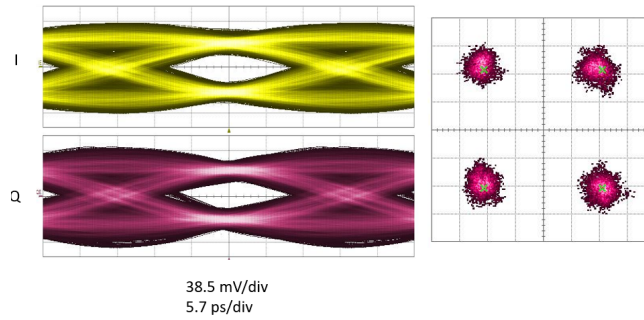


Figure 6.12: Received eye diagram and IQ constellation of a 28 GBd QPSK transmission with LO at 152 GHz and  $\text{BER} < 10^{-12}$  over a 1 m PMF.

The BER for different baud rates for QPSK modulation was measured all the way up to 40 Gbd, corresponding to 80 Gbps. The result can be seen in Fig. 6.13. The bandwidth of the AWG is only 32 GHz, and the bandwidth of the oscilloscope is 36 GHz which means that this is also a limitation during the measurement.

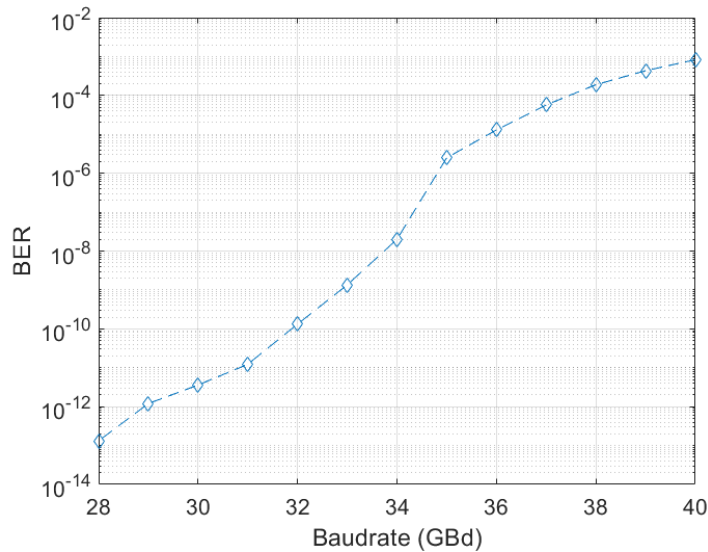


Figure 6.13: BER for different baud rates for QPSK modulation.

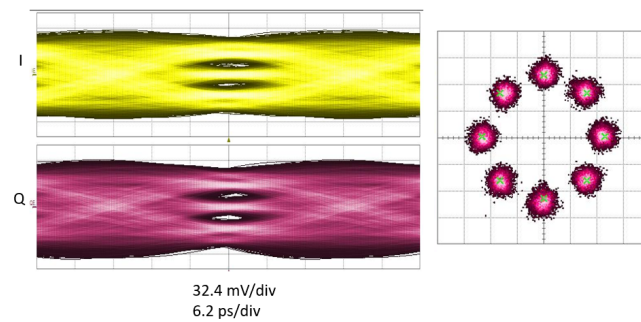
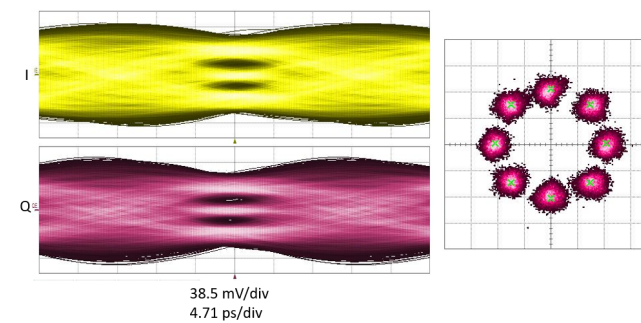
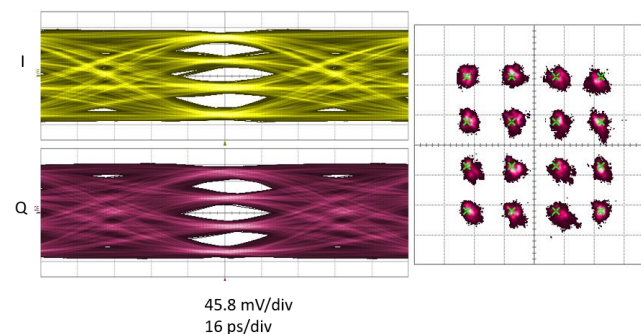
8-PSK modulation was also investigated. I/Q constellation and Eye diagram for 8-PSK modulation can be seen in Fig. 6.14 and 6.15 for data rates of 26 GBd (78 Gbps) and 34 GBd (102 Gbps).

Error rate is increased, but clear constellations can be seen, breaking the 100 Gbps goal. Transmissions with QAM-16 modulations were also tested. In Fig. 6.16 10 GBd is transmitted, corresponding to 40 Gbps.

The DC power consumption for the Tx is 437 mW, and for the Rx, it is 556 mW.

In Paper H longer links were evaluated, using a two meter and a four meter long PMF. A photo of the setup with the two meter long PMF can be seen in Fig. 6.17.

In the link measurement a carrier frequency of 148 GHz was used. QPSK modulation was tested at a baud rate of 24 GBd corresponding to 48 Gbps. Captured

Figure 6.14: 26 GBd 8-PSK with LO at 151 GHz and  $\text{BER}=2.9 \cdot 10^{-4}$ .Figure 6.15: 34 GBd 8-PSK with LO at 151 GHz and  $\text{BER}=2.1 \cdot 10^{-3}$ .Figure 6.16: 10 GBd QAM-16 with LO at 153 GHz and  $\text{BER}=2.4 \cdot 10^{-8}$ .

eye diagram and I/Q constellation can be seen in Fig. 6.18.

## 6.4 Comparison with similar work

In Table 6.1 the performance of a few similar links are presented, as well as links based on work in this thesis for comparison. For a fair comparison only links achieving a BER of less than  $10^{-12}$  are included.

Compared to similar work in Table 6.1, the highest datarate is achieved using an I/Q modulated Tx and Rx. Complexity is increased and carrier recovery is needed, thus increasing power consumption and chip size. The PAM modulated links are

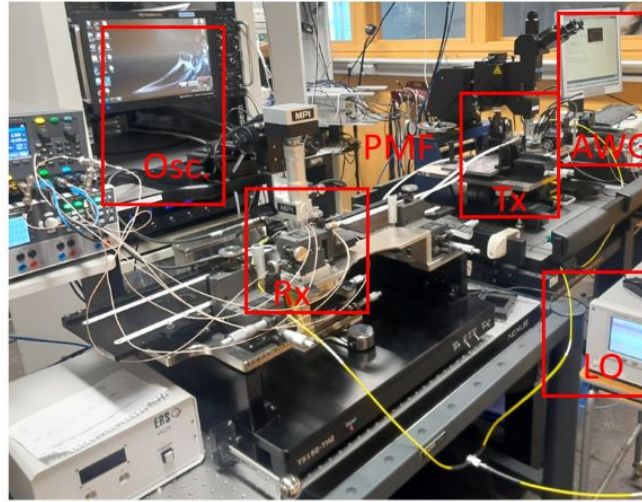


Figure 6.17: A photo of the setup for the link measurements using a two meter long PMF.

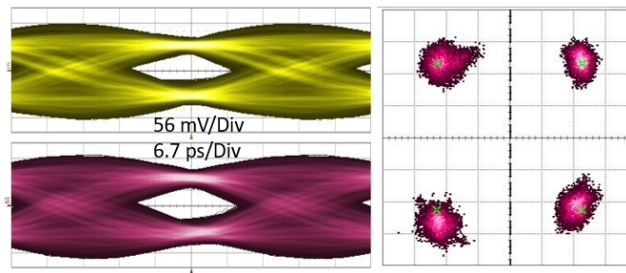


Figure 6.18: Received eye diagram and I/Q constellation of a 24 GBd QPSK transmission over a two meter PMF. LO at 148 GHz and BER  $< 10^{-12}$ .

Table 6.1: Comparison with other links, with BER  $< 10^{-12}$

Ref.	[33]	[6]	[19]	[7]	C	D	F	G	H
<b>Technology</b>	40nm CMOS	28nm CMOS	65nm CMOS	28nm CMOS	250nm InP DHBT	130nm BiCMOS	130nm BiCMOS	130nm BiCMOS	130nm BiCMOS
<b>Modulation</b>	CP-FSK	CP-FSK	ASK	PAM-4	PAM-2	PAM-4	QPSK	QPSK	QPSK
<b>Frequency (GHz)</b>	120	140	60	135	131	138	148	152	148
<b>Data Rate (Gbps)</b>	17.7	12	6	27					
<b>Fiber Length (m)</b>	1.0	1.0	2.0	1.0	1.0	1.0	1.0	1.0	2.0
<b>Energy Eff. (pJ/bit)</b>	4.0*	19.2	4.7	4.8	4.1*	9.55*	47*	17.7*	24.7*
*no LO included									
<b>Total chip area (mm<sup>2</sup>)</b>	N/A	2.31	N/A	1.94	0.83	1.54	4.2	4.2	4.2

energy efficient, and small in size. Both of the types of links has demonstrated some of the highest and the highest data rate by far.

# Chapter 7

## Conclusion and Future Outlook

### 7.1 Conclusion

In this work, different solutions for high data rate communication have been presented. The emitter-coupled RF-DAC has demonstrated great potential for speed, while the stacked topology was a strong competitor for its low DC power consumption.

The topologies investigated for the PDs were based on using baluns at the input to suppress the fundamental frequency. Both passive and active baluns were tested with similar performance.

The RF-DAC based transmitters and PDs have demonstrated up to 30 Gbps error-free ( $\text{BER} < 10^{-12}$ ) data transmissions in real-time. The benefit of not having to use signal synchronization makes it a good option when circuit size and energy efficiency are vital.

Comparing the technologies used, Teledyne's InP DHBT process is extremely powerful with a higher ( $f_t$  and  $f_{\max}$ ), but the circuits are more fragile compared to Infineon's SiGe BiCMOS process.

More understanding of the dispersive effects of the PMF on a signal, provided insights that a higher carrier frequency is desirable for broadband signals to avoid symbol interference. Pulse shaping and equalization were successfully used to achieve a higher data rate.

The integrated I/Q modulated links require more complexity, larger area and higher DC power consumption, but a higher data rate was reached, demonstrating over 100 Gbps using 8-PSK. Error-free ( $\text{BER} < 10^{-12}$ ) communication using QPSK reached 56 Gbps, which is more than double compared to other work.

### 7.2 Future Outlook

Future work includes further development of the RF-DAC/PD PMF communication link, to reach a higher data rate. The plan is to move up in frequency to G-band (140 GHz - 220 GHz), Y-band (170 GHz - 260 GHz) and H-band (220 GHz - 325 GHz). Areas to focus on are bandwidth, power consumption and output power. Integration of more components, like comparators at the receiver, to be able to get a bit stream

as output. Further exploring options on how to deal with the dispersive effects of the fiber on the signal.

The I/Q modulated link has a larger bandwidth than the measurement equipment at the moment. The next step to further increase the data rate is likely to improve the SNR to be able to have a higher modulation order. The cross-talk between the I and Q channel needs to be addressed through for example, physical separation of the channels, fine-tuning of baluns/hybrids, and circuitry to compensate for the cross-talk. LO leakage can be eliminated by adding a DC bias at the I/Q ports. Output power can also further be improved.

# Chapter 8

## Summary of Appended Papers

### Paper A

#### **A RF-DAC based 40 Gbps PAM Modulator with 1.2 pJ/bit Energy Efficiency at Millimeterwave Band**

A PAM-4 modulator is designed and fabricated in a  $0.25\ \mu\text{m}$  indium phosphide (InP) double heterojunction bipolar transistor (DHBT) technology. The modulator is verified to have a 3-dB bandwidth of 60-90 GHz and a peak output power of -5 dBm at 75 GHz. This modulator can support 40 Gbps data transmission with a bit error rate of  $3.7 \times 10^{-6}$ , the energy efficiency is better than 1.2 pJ/bit. This modulator is suitable for application such as low power, short range, ultra high data rate wireless communication.

##### **My contributions:**

- Designed the circuit
- Did the literature research
- Performed theoretical analysis
- Built the experimental setup with co-authors
- Did the measurement with co-authors
- Analyzed the data and wrote the paper with co-authors

### Paper B

#### **Multi-Gigabit RF-DAC Based Duobinary/PAM-3 Modulator in 130 nm SiGe HBT**

In this work a combined duobinary and PAM-3 (Pulse Amplitude Modulation) modulator is designed and fabricated using a 130 nm silicon germanium process. The

RF-DAC based duobinary/PAM-3 modulator covers 95 GHz of bandwidth between 35 GHz and 130 GHz and uses three-valued logic. Together with a power detector, high data rate links can be realized without carrier recovery or phase recovery, thus simplifying the overall design. Data rates up to 30 Gbps is demonstrated using duobinary modulation with a symbol error rate (SER) of  $6.4 * 10^{-6}$ . For PAM-3 modulation data rates up to 28 Gbps is demonstrated with a SER of  $1.4 * 10^{-6}$ . The wide bandwidth and high data rate makes it suitable to be used together with a polymer microwave fiber (PMF) for a low cost and robust system, instead of optic fiber.

**My contributions:**

- Designed the circuit
- Did the literature research
- Performed theoretical analysis
- Built the experimental setup
- Did the measurement
- Analyzed the data and wrote the paper

## Paper C

### Transmitter and Receiver Circuits for a High-speed Polymer-fiber based PAM-4 Communication Link

A high data rate RF-DAC and power detector (PD) are designed and fabricated in a 250 nm indium phosphide (InP) double heterojunction bipolar transistor (DHBT) technology. A communication link using the Tx-Rx over polymer microwave fiber (PMF) is measured. The link consists of a pulse amplitude modulation (PAM) modulator, and a PD as a demodulator, as well as a one meter long dielectric waveguide. The working frequency range of the complete link is verified to be 110 - 150 GHz. The peak output power of the PAM-modulator is 5 dBm and it has a -3 dB bandwidth of 43 GHz. The PD consists of a parallel connected common emitter configured transistor and a common base configured transistor to suppress the odd-order harmonics at the PD's output, as well as a stacked transistor to amplify the output signal. Tx and Rx chips, including pads, occupy an area of only 0.83 mm<sup>2</sup> totally. The PMF link can support a PAM-4 signal with a 22 Gbps data transmission, and a PAM-2 signal with 30 Gbps data transmission, with a bit error rate (BER) of  $< 10^{-12}$ , with demodulation done in real time. Furthermore, the energy efficiency for the link (Tx + Rx) is 4.1 pJ/bit, using digital data input and receiving PAM-2 output (5.6 pJ/bit for PAM-4).

**My contributions:**

- Designed the transmitter circuit (receiver was designed by Mingquan Bao)

- Did the literature research
- Performed theoretical analysis
- Built the experimental setup
- Did the measurement
- Analyzed the data and wrote the paper

## Paper D

### Transmitter and Receiver for High Speed Polymer Microwave Fiber Communication at D-band

A chipset for high datarate polymer microwave fiber (PMF) communication is described. It consist of a PAM-4 RF-DAC and power detector (PD) and is fabricated using a commercial 130 nm SiGe BiCMOS process. A link measurement is performed over a one meter long PMF verifying that the link can support data rates up to 20 Gbps using PAM-4, with a bit error rate (BER) of  $< 10^{-12}$ . The RF-DAC covers frequencies between 120-160 GHz, with a peak output power of 4 dBm. It has a stacked transistor pair as core and includes a frequency doubler at the LO input and a three stage amplifier at the output. The PD includes an amplifier and an active balun to suppress the fundamental frequency. Both circuits occupy only 1.54 mm<sup>2</sup> combined, including pads. The high data-rate, energy efficiency, low cost and robustness of the link makes is suitable for short range ( $< 10$  meters) device-to-device communication.

#### **My contributions:**

- Designed the frequency doubler, RF-DAC core and power detector
- Integrated transmitter and receiver (Herbert Zirath's amplifier is integrated in the circuits)
- Did the literature research
- Performed theoretical analysis
- Built the experimental setup
- Did the measurement
- Analyzed the data and wrote the paper

## Paper E

### A PAM-4 Link for High Data Rate PMF Communication

In this work a high speed PAM-4 link for polymer microwave fiber (PMF) communication at D-band (110-170GHz) is presented using a commercial 130 nm SiGe BiCMOS process. Link measurements are performed over a one meter long foam-cladded PMF which verifies that the link can support data rates up to 30 Gbps with a bit error rate (BER) of  $3 * 10^{-8}$ . The transmitter is RF-DAC based including an LO multiplier and a six stage amplifier. The receiver consists of an LNA and a power detector (PD). The DC power consumption is 143 mW for the transmitter and 126 mW for the receiver.

#### My contributions:

- Designed the frequency doubler, RF-DAC core and power detector
- Integrated transmitter and receiver (Herbert Zirath's amplifier is integrated in the circuits)
- Did the literature research
- Performed theoretical analysis
- Built the experimental setup
- Did the measurement
- Analyzed the data and wrote the paper

## Paper F

### A 40 Gbps QAM-16 communication link using a 130 nm SiGe BiCMOS process

In this work a high data rate transmitter and receiver link is presented using a 130 nm SiGe BiCMOS process. The communication link has demonstrated transmissions up to 40 Gbps QAM-16 at D-band (110-170 GHz) over a one meter polymer microwave fiber (PMF). The peak output power of the transmitter (Tx) is 3 dBm at 135 GHz and the 3-dB bandwidth of both Tx and receiver (Rx) is between 115 - 145 GHz, resulting in a 30 GHz bandwidth. Total chip area for Tx and Rx combined, including pads, is 4.2 mm<sup>2</sup>.

#### My contributions:

- Designed the frequency quadrupler
- Integrated transmitter and receiver (Herbert Zirath's amplifier and Yu Yan's mixers are integrated in the circuits)

- Did the literature research
- Performed theoretical analysis
- Built the experimental setup
- Did the measurement
- Analyzed the data and wrote the paper

## Paper G

### **A Beyond 100 Gbps Polymer Microwave Fiber Communication Link at D-band**

A D-band (110-170 GHz) ultra high data rate link is presented and characterized. The circuits are realized in a commercial 130 nm silicon germanium (SiGe) BiCMOS process. The 3-dB bandwidth for both transmitter (Tx) and receiver (Rx) is between 125 - 165 GHz, resulting in a 40 GHz bandwidth. The communication link has demonstrated transmissions up to 102 Gbps using 8-phase shift keying (PSK) modulation over a one meter long foam-cladded polymer microwave fiber (PMF) with a bit error rate (BER) of  $2.1 \times 10^{-3}$ . Using direct quadrature phase shift keying (QPSK), 56 Gbps was reached with a BER  $< 10^{-12}$ . Total chip area for Tx and Rx combined, including pads, is 4.2 mm<sup>2</sup>.

#### **My contributions:**

- Designed the frequency quadrupler
- Integrated transmitter and receiver (Herbert Zirath's amplifier and Yu Yan's mixers are integrated in the circuits)
- Did the literature research
- Performed theoretical analysis
- Built the experimental setup
- Did the measurement
- Analyzed the data and wrote most of the paper

## Paper H

### **An 80 Gbps QAM-16 PMF Link Using a 130 nm SiGe BiCMOS Process**

In this work a D-band (110 GHz - 170 GHz) polymer microwave fiber (PMF) link for high data rate communication is presented. The transmitter (Tx) and receiver

(Rx) circuits are designed and fabricated in a commercial 130 nm silicon germanium (SiGe) BiCMOS process. The Tx has a peak output power of 5 dBm. The link has been tested over a 2 meter long PMF, demonstrating 80 Gbps using QAM-16 modulation, with a bit error rate (BER) of  $8 * 10^{-4}$ , and 48 Gbps using QPSK with a BER  $< 10^{-12}$ . For a 4 meter long PMF, 24 Gbps using QPSK was demonstrated with a BER =  $7.7 * 10^{-6}$ .

**My contributions:**

- Designed the frequency quadrupler
- Integrated transmitter and receiver (Herbert Zirath's amplifier and Yu Yan's mixers are integrated in the circuits)
- Did the literature research
- Performed theoretical analysis
- Built the experimental setup
- Did the measurement
- Analyzed the data and wrote the paper

# Bibliography

- [1] Jochen Antes and Ingmar Kallfass. “Performance Estimation for Broadband Multi-Gigabit Millimeter-and Sub-Millimeter-Wave Wireless Communication Links”. In: *IEEE Transactions on Microwave Theory and Techniques* 63 (10 2015). ISSN: 00189480. DOI: 10.1109/TMTT.2015.2467390 (cit. on p. 47).
- [2] M. Bao, J. Chen, R. Kozhuharov, and H. Zirath. “14 Gbps on-off keying modulator and demodulator for D-band communication”. In: *Proc. IEEE Int. Wireless Symp. (IWS 2014)*. Mar. 2014, pp. 1–4. DOI: 10.1109/IEEE-IWS.2014.6864208 (cit. on p. 31).
- [3] J. Böck et al. “SiGe HBT and BiCMOS process integration optimization within the DOTSEVEN project”. In: vol. 2015-November. 2015. DOI: 10.1109/BCTM.2015.7340549 (cit. on p. 21).
- [4] Kai Chang. *RF and Microwave Wireless Systems*. 2000. DOI: 10.1002/0471224324 (cit. on p. 6).
- [5] S. Cherry. “Edholm’s law of bandwidth”. In: *IEEE Spectrum* 41.7 (2004), pp. 58–60. DOI: 10.1109/MSPEC.2004.1309810 (cit. on p. 1).
- [6] M. De Wit, Y. Zhang, and P. Reynaert. “Analysis and Design of a Foam-Cladded PMF Link With Phase Tuning in 28-nm CMOS”. In: *IEEE Journal of Solid-State Circuits* 54.7 (July 2019), pp. 1960–1969. ISSN: 1558-173X. DOI: 10.1109/JSSC.2019.2907163 (cit. on p. 60).
- [7] Kristof Dens, Joren Vaes, Simon Ooms, Martin Wagner, and Patrick Reynaert. “A PAM4 Dielectric Waveguide Link in 28 nm CMOS”. In: 2021. DOI: 10.1109/ESSCIRC53450.2021.9567741 (cit. on p. 60).
- [8] Ke Lin Du and M. N.S. Swamy. *Wireless communication systems: From RF subsystems to 4G enabling technologies*. 2010. DOI: 10.1017/CB09780511841453 (cit. on p. 11).
- [9] H.T. Friis. “Noise Figures of Radio Receivers”. In: *Proceedings of the IRE* 32.7 (1944), pp. 419–422. DOI: 10.1109/JRPR0C.1944.232049 (cit. on p. 5).
- [10] B. Gilbert. “A precise four-quadrant multiplier with subnanosecond response”. In: *IEEE Journal of Solid-State Circuits* 3.4 (1968), pp. 365–373. DOI: 10.1109/JSSC.1968.1049925 (cit. on p. 40).
- [11] Qun Jane Gu. “THz interconnect: the last centimeter communication”. In: *IEEE Communications Magazine* 53.4 (2015), pp. 206–215. DOI: 10.1109/MCOM.2015.7081096 (cit. on p. 2).

- [12] Jonathan Hacker, Miguel Urteaga, Munkyo Seo, Anders Skalare, and Robert Lin. “InP HBT amplifier MMICs operating to 0.67 THz”. In: 2013. DOI: 10.1109/MWSYM.2013.6697518 (cit. on p. 2).
- [13] Jack W. Holloway, Georgios C. Dogiamis, and Ruonan Han. “A 105Gb/s Dielectric-Waveguide Link in 130nm BiCMOS Using Channelized 220-to-335GHz Signal and Integrated Waveguide Coupler”. In: vol. 64. 2021. DOI: 10.1109/ISSCC42613.2021.9365857 (cit. on p. 25).
- [14] François Horlin and André Bourdoux. *Digital Compensation for Analog Front-Ends: A New Approach to Wireless Transceiver Design*. 2008. DOI: 10.1002/9780470759028 (cit. on p. 47).
- [15] Billington J. *Connectivity challenges for next-generation autonomous cars*. 2018. URL: <https://www.autonomousvehicleinternational.com/opinion/connectivity.html> (cit. on p. 3).
- [16] Clement J. *Internet usage worldwide - Statistics & Facts | Statista*. 2020. URL: <https://www.statista.com/topics/1145/internet-usage-worldwide/> (cit. on p. 1).
- [17] M. Reza Khanzadi, Dan Kuylenstierna, Ashkan Panahi, Thomas Eriksson, and Herbert Zirath. “Calculation of the performance of communication systems from measured oscillator phase noise”. In: *IEEE Transactions on Circuits and Systems I: Regular Papers* 61 (5 2014). ISSN: 15498328. DOI: 10.1109/TCSI.2013.2285698 (cit. on p. 47).
- [18] Y. Kim, B. Hu, Y. Du, R. Huang, R. Al-Hadi, A. Tang, H. Chen, C. Jou, T. Itoh, and M. F. Chang. “30Gb/s 60.2mW 151GHz CMOS Transmitter/Receiver with Digitally Pre-Distorted Current Mode PAM-4 Modulator for Plastic waveguide and Contactless Communications”. In: *Proc. IEEE MTT-S Int. Microwave Symp. (IMS)*. June 2019, pp. 673–676. DOI: 10.1109/MWSYM.2019.8701006 (cit. on p. 25).
- [19] Y. Kim, L. Nan, J. Cong, and M. F. Chang. “High-Speed mm-Wave Data-Link Based on Hollow Plastic Cable and CMOS Transceiver”. In: *IEEE Microwave and Wireless Components Letters* 23.12 (Dec. 2013), pp. 674–676. ISSN: 1558-1764. DOI: 10.1109/LMWC.2013.2283862 (cit. on p. 60).
- [20] Thomas Kürner and Sebastian Priebe. “Towards THz communications - Status in research, standardization and regulation”. In: *Journal of Infrared, Millimeter, and Terahertz Waves* 35 (1 2014). ISSN: 18666906. DOI: 10.1007/s10762-013-0014-3 (cit. on p. 2).
- [21] R. R. Mahmud, M. A.G. Khan, and S. M.A. Razzak. “Design of a duobinary encoder and decoder circuits for communication systems”. In: 2010. DOI: 10.1109/ICELCE.2010.5700550 (cit. on p. 28).
- [22] S. Marsh. *Practical MMIC Design*. Artech House microwave library. Artech House, 2006. ISBN: 9781596930360 (cit. on p. 22).

- [23] Sanaz Mortazavi, Detlef Schleicher, and Friedel Gerfers. “Modeling and Verification of Automotive Multi-Gig Ethernet Communication up to 2.5 Gbps and the Corresponding EMC Analysis”. In: 2018. ISBN: 9781538666210. DOI: 10.1109/EMCSI.2018.8495375 (cit. on p. 28).
- [24] Hyunsu Park, Junyoung Song, Yeonho Lee, Jincheol Sim, Jonghyuck Choi, and Chulwoo Kim. “23.3 A 3-bit/2UI 27Gb/s PAM-3 Single-Ended Transceiver Using One-Tap DFE for Next-Generation Memory Interface”. In: vol. 2019-February. 2019. DOI: 10.1109/ISSCC.2019.8662462 (cit. on p. 28).
- [25] P. Reynaert, M. Tytgat, W. Volkaerts, A. Standaert, Y. Zhang, M. De Wit, and N. Van Thienen. “Polymer Microwave Fibers: A blend of RF, copper and optical communication”. In: *Proc. ESSCIRC Conf. 2016: 42nd European Solid-State Circuits Conf.* Sept. 2016, pp. 15–20. DOI: 10.1109/ESSCIRC.2016.7598233 (cit. on pp. 7, 25).
- [26] Patrick Reynaert, Kristof Dens, Carl D’Heer, Dragan Simic, Joren Vaes, Bart Philippe, and Simon Ooms. “Polymer microwave fiber: A new communication concept that blends wireless, wireline and optical communication”. In: 2019. DOI: 10.1109/ICECS46596.2019.8964776 (cit. on p. 7).
- [27] Claude E. Shannon. “A Mathematical Theory of Communication”. In: *Claude E. Shannon: Collected Papers.* 1993, pp. 5–83. DOI: 10.1109/9780470544242.ch1 (cit. on p. 2).
- [28] Ho-Jin Song and Tadao Nagatsuma. “Present and Future of Terahertz Communications”. In: *IEEE Transactions on Terahertz Science and Technology* 1.1 (2011), pp. 256–263. DOI: 10.1109/TTHZ.2011.2159552 (cit. on p. 2).
- [29] National Telecommunications and Information Administration. 2016. URL: <https://www.ntia.doc.gov/page/2011/united-states-frequency-allocation-chart> (cit. on p. 2).
- [30] Inc. Teledyne LeCroy. *Instruction Manual - VectorLinQ - Vector Signal Analysis Software.* 2016. URL: <http://cdn.teledynelecroy.com/files/manuals/vectorlinq-software-instruction-manual.pdf> (cit. on p. 54).
- [31] M. Tytgat and P. Reynaert. “A plastic waveguide receiver in 40nm CMOS with on-chip bondwire antenna”. In: *Proc. ESSCIRC (ESSCIRC) 2013.* Sept. 2013, pp. 335–338. DOI: 10.1109/ESSCIRC.2013.6649141 (cit. on p. 25).
- [32] N. Van Thienen, W. Volkaerts, and P. Reynaert. “A Multi-Gigabit CPFSK Polymer Microwave Fiber Communication Link in 40 nm CMOS”. In: *IEEE Journal of Solid-State Circuits* 51.8 (Aug. 2016), pp. 1952–1958. ISSN: 1558-173X. DOI: 10.1109/JSSC.2016.2580605 (cit. on p. 25).
- [33] N. Van Thienen, Y. Zhang, M. De Wit, and P. Reynaert. “An 18Gbps polymer microwave fiber (PMF) communication link in 40nm CMOS”. In: *Proc. ESSCIRC Conf. 2016: 42nd European Solid-State Circuits Conf.* Sept. 2016, pp. 483–486. DOI: 10.1109/ESSCIRC.2016.7598346 (cit. on p. 60).
- [34] Sorin Voinigescu. *High-Frequency Integrated Circuits.* 2013. DOI: 10.1017/cbo9781139021128 (cit. on p. 26).

- [35] W. Volkaerts, N. Van Thienen, and P. Reynaert. “An FSK plastic waveguide communication link in 40nm CMOS”. In: *Proc. IEEE Int. Solid-State Circuits Conf. - (ISSCC) Digest of Technical Papers*. Feb. 2015, pp. 1–3. DOI: 10.1109/ISSCC.2015.7062984 (cit. on p. 25).
- [36] C. Yeh and F. I. Shimabukuro. *The essence of dielectric waveguides*. 2008. DOI: 10.1007/978-0-387-49799-0 (cit. on p. 7).

# Acknowledgments

First and foremost, I would like to thank my supervisor Prof. Herbert Zirath. Without your enormous patience and support this work would not have been possible. You have given me so much freedom and trust to let me develop as a circuit designer. You truly understand my passion for circuit design.

Working on integrations with Dr. Yu Yan is not only easy and rewarding but also a lot of fun. We are a great team, and we always manage to finish every tapeout (I still don't know how).

Enormous thanks to Assoc. Prof. Zhongxia Simon He. You always believe in me, even when things are difficult.

I want to thank Dr. Mingquan Bao for sharing some of his knowledge and inspiration to be a brave circuit designer and Assoc. Prof. Dan Kuylenstierna for giving me new challenges. Assoc. Prof Vessen Vassilev, you're always there to help me discuss my measurement setup, even though I don't work with you. I would also like to thank Prof. Jan Stake for his support. Prof. Ilcho Angelov, you will always be someone I look up to.

Microwave Electronics Laboratory head Prof. Christian Fager is always spreading happiness, and I am sorry I always have to finish my tapeouts during conferences, but it is actually not my fault.

My gratitude also goes to Infineon Technologies and Teledyne Scientific Company for the fabrication of the circuits (that are used in this thesis).

To my colleagues (former and present) and friends; Ahmed, Olivier, Juan, Sining, Ibrahim, Stavros, Martin, José, Thanh, Han, Gregor, Rob, and Göksu, as well as many more, you truly make my days better. I am thankful that you guys still put up with me.

Last but not least, I would like to thank my family, as well as my cat Mufasa and my horses. You always make me keep going. I don't know how often Lotta Strömbeck and Timo Paulsson have been there, giving me advice and support, talking late into the night (and bringing breakfast in the morning). From horse riding, I have learned that even if you fall, it's not a failure unless you give up.

Frida Strömbeck  
Göteborg, February 2023

